

SYNERGETIC EFFECTS OF NANO-SIZED ZINC OXIDE OBTAINED
FROM VARIOUS SOURCES AND CARBONACEOUS MATERIALS IN
ENERGY STORAGE SYSTEMS

by
EGEHAN ERÇAY

Submitted to the Graduate School of Engineering for Natural Sciences
in partial fulfillment
of the requirements for the degree of
Master of Science

Sabancı University

December 2023

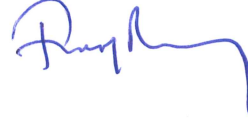
SYNERGETIC EFFECTS OF NANO-SIZED ZINC OXIDE OBTAINED
FROM VARIOUS SOURCES AND CARBONACEOUS MATERIALS IN
ENERGY STORAGE SYSTEMS

APPROVED BY:

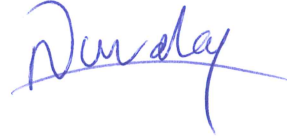
Prof. Dr. Emre Erdem
(Thesis Supervisor)



Assoc. Prof. Dr. Feray Bakan Mısırlıoğlu



Prof. Dr. Nurdan Demirci Sankır



DATE OF APPROVAL: 25.12.2023

© Egehan Erçay 2023
All Rights Reserved

ABSTRACT

SYNERGETIC EFFECTS OF NANO-SIZED ZINC OXIDE OBTAINED FROM VARIOUS SOURCES AND CARBONACEOUS MATERIALS IN ENERGY STORAGE SYSTEMS

EGEHAN ERÇAY

Materials Science and Nanoengineering M.Sc. Thesis December 2023

Supervisor: Prof. Dr. Emre Erdem

Keywords: sol-gel method, supercapacitor, zinc oxide, nanoparticles

In recent years, the escalating global demand for sustainable and efficient energy storage solutions has propelled supercapacitors to the forefront of research and development in the field of advanced energy storage systems. With their unique ability to deliver rapid charge and discharge cycles, coupled with an extended operational lifespan, supercapacitors represent a promising alternative to conventional energy storage technologies. Investigation in this thesis includes Zinc Oxide (ZnO) supercapacitors, synthesized through the sol-gel method which have undergone comprehensive testing to evaluate their structural integrity and electrochemical properties, providing crucial insights into their performance and potential applicability in advanced energy storage systems. Morphological characteristics of the ZnO powders produced were investigated through X-Ray Diffraction (XRD) and Scanning Electron Microscopy (SEM) analyses. Among the nanoparticles, ZA/HBA exhibited the highest crystallinity at 84.2%. Defect structures in the nanoparticles were identified via Photoluminescence Spectroscopy (PL) and analyzed using Electron Paramagnetic Resonance Spectroscopy (EPR) for both intrinsic and extrinsic defects in synthesized zinc oxide nanoparticles. Specific capacitance evaluations, spanning a 10mV/s to 200mV/s scan rate using a Potentiostat, demonstrated superior electrochemical properties in asymmetrical supercapacitors, where sol-gel-produced zinc oxide and active carbon served as electrodes, compared to symmetrical counterparts. Values for specific capacitance, energy density, and power density achieved notable levels, reaching up to 92.8 F g⁻¹, 12.9 Wh kg⁻¹, and 4231.6 kW kg⁻¹, respectively. These results exhibit significant potential compared to existing literature, indicating the possibility of further improvements by introducing additional electrochemically active materials on the opposing side of the electrode in asymmetrical supercapacitors.

ÖZET

Son yıllarda, sürdürülebilir ve verimli enerji depolama çözümlerine olan küresel talebin artması, süperkapasitörleri ileri enerji depolama sistemleri alanındaki araştırma ve geliştirmenin ön saflarına taşımıştır. Hızlı şarj ve deşarj döngülerini sunma yetenekleri ve uzatılmış operasyonel ömürleri ile, süperkapasitörler geleneksel enerji depolama teknolojilerine vaat edici bir alternatif oluşturmaktadır. Bu tezdeki inceleme, sol-jel yöntemiyle sentezlenen Çinko Oksit (ZnO) süperkapasitörlerini içermekte olup, yapısal bütünlüklerini ve elektrokimyasal özelliklerini değerlendirmek için kapsamlı testlere tabi tutulmuşlardır, bu da ileri enerji depolama sistemlerindeki potansiyel uygulamaları hakkında kritik bilgiler sağlamaktadır. Üretilen ZnO tozlarının morfolojik özellikleri X-ışını Difraksiyonu (XRD) ve Taramalı Elektron Mikroskobu (SEM) analizleri ile incelenmiştir. Nanopartiküller arasında ZA/HBA, %84.2 ile en yüksek kristallliği sergilemiştir. Nanomalzemelerdeki hata yapıları, Fotolüminesans Spektroskopisi (PL) ile belirlenmiş ve hem içsel hem de dışsal hatalar için Elektron Paramanyetik Rezonans Spektroskopisi (EPR) kullanılarak analiz edilmiştir. Potentiostat kullanılarak 10mV/s ile 200mV/s tarama hızı arasında yapılan özgül kapasitans değerlendirmeleri, sol-jel yöntemi ile üretilen çinko oksit ve aktif karbonun elektrot olarak kullanıldığı asimetrik süperkapasitörlerde, simetrik karşılıklarına kıyasla üstün elektrokimyasal özellikler göstermiştir. Özgül kapasitans, enerji yoğunluğu ve güç yoğunluğu için değerler, sırasıyla 92.8 F g⁻¹, 12.9 Wh kg⁻¹ ve 4231.6 kW kg⁻¹'e kadar çıkan önemli seviyelere ulaşmıştır. Bu sonuçlar, mevcut literatüre kıyasla önemli bir potansiyel sergilemekte, asimetrik süperkapasitörlerde elektrodun karşı tarafına ek elektrokimyasal olarak aktif malzemeler ekleyerek daha fazla iyileştirmelerin mümkün olduğunu göstermektedir.

ACKNOWLEDGEMENT

I would like to start with a heartfelt gratitude for my supervisor, Prof. Dr. Emre Erdem, whose expertise, understanding, and patience, added considerably to my graduate experience. His willingness to give his time so generously has been very much appreciated. He was always available and motivational even through times that was hard for me to concentrate. I have been amazingly fortunate to have an advisor who gave me the freedom to explore on my own, while at the same time ensuring I stayed on track.

Moreover, I really appreciate the opportunity that was given to me by Sabancı University to conduct this research and thesis. It was an enjoyable journey which enabled me to challenge myself for always improving.

I am also grateful to the professors of my thesis committee, Assoc. Prof. Dr. Feray Bakan Mısırlıoğlu & Prof. Dr. Nurdan Sankır, who gave their time and effort to read and evaluate this thesis. My thanks also go out to my friends and fellow researchers Mohamad Hasan Aleinawi, Merve Aktürk, Ameenuddin Ammar, Ahmet Güngör, Abdalla Hroub, Ipek Deniz Yıldırım, and Sumaiyah Najib for all the stimulating conversations, and great memories.

Finally, I must express my very profound gratitude to my family for providing me with unfailing support and continuous encouragement throughout my years of study and through the process of researching and writing this thesis. This accomplishment would not have been possible without them. Thank you. This thesis stands as a milestone in my academic journey, and I am grateful for everyone who has made it possible.

TABLE OF CONTENTS

ABSTRACT	I
ÖZET	II
TABLE OF CONTENTS	IV
LIST OF FIGURES	V
LIST OF TABLES	VI
1. INTRODUCTION	1
2. MATERIALS AND METHODS	10
2.1 Materials	10
2.2 Synthesis of Nanoparticles with Sol-Gel Method	10
2.3 Production of Supercapacitors	13
2.4 Characterizations	16
3. RESULTS AND DISCUSSION	19
3.1 X-ray Diffraction (XRD) Analysis	19
3.2 Scanning Electron Microscopy (SEM) Analysis	22
3.3 Raman Spectroscopy Analysis	24
3.4 Photoluminescent (PL) Spectroscopy Analysis	26
3.5 Electron Paramagnetic Resonance (EPR) Spectroscopy Analysis	30
4. ELECTROCHEMICAL ANALYSIS	32
5. CONCLUSIONS	40
6. REFERENCES	42

LIST OF FIGURES

Fig. 1: Schematic diagram of analysis procedures of ZnO nanoparticles.	5
Fig. 2: Schematic diagram for experimental procedures of ZnO nanoparticles and drying, calcination temperatures- time values.	11
Fig. 3: Supercapacitor mounting device that was used in this thesis[49].	13
Fig. 4: Energy schema for Zeeman splitting [29].	17
Fig. 5: Rietveld Refinement for sample ZA/TA.	20
Fig. 6: SEM with 10.00 KX and 30.00 KX magnification of ZA/TA (a), ZN/TA (b), ZA/Ch (c), ZA/AA (d), ZA/HBA (e) nanoparticles.	22
Fig. 7: First-order and second-order Raman spectrum of the synthesized particles ($\lambda = 532$ nm). The alterations in the vibration bands in the range of $125-2000\text{ cm}^{-1}$ are given.	24
Fig. 8: PL spectra of ZnO samples ZA/TA, ZN/TA, ZA/Ch, ZA/AA, ZA/HBA	27
Fig. 9: PL spectra of ZA/TA with deconvolution	27
Fig. 10: PL spectra of ZN/TA with deconvolution	28
Fig. 11: PL spectra of ZN/Ch with deconvolution	28
Fig. 12: PL spectra of ZN/AA with deconvolution	29
Fig. 13: PL spectra of ZN/HBA with deconvolution	29
Fig. 14: EPR spectroscopy analysis of ZA/TA (a), ZN/TA (b), ZA/Ch (c), ZA/AA (d) and ZA/HBA (e).	30
Fig. 15: Electrochemical impedance spectra (Nyquist plot) of supercapacitor designs.	33
Fig. 16: CV Graph for symmetric supercapacitors at 200mV/s scan rate	33
Fig. 17: CV Graph for symmetric bulk ZnO supercapacitors at various scan rates	34
Fig. 18: CV Graph for symmetric nano ZnO supercapacitors at various scan rates	34
Fig. 19: CV Graph for asymmetric bulk ZnO supercapacitors at various scan rates	34
Fig. 20: CV Graph for asymmetric nano ZnO supercapacitors at various scan rates	34
Fig. 21: CV graph for ZA/HBA/AC asymmetric supercapacitor.	36
Fig. 22: CV graph for ZN/TA/AC asymmetric supercapacitor.	36
Fig. 23: Z-Fit graphs for samples ZA/TA, ZN/TA, ZA/Ch, ZA/AA, and ZA/HBA.	37

LIST OF TABLES

Table. 1 Powder samples, chemical compositions, starting materials, solvents, stirring, drying and calcination parameters used for the synthesis.....	12
Table. 2 Symmetric supercapacitor samples, mass of two electrodes. Also, electrolyte and separator names were given for the supercapacitor analysis of different ZnO nanoparticles.	15
Table. 3 Percentage of crystallinity and amorphous values of different ZnO nanoparticles.	20
Table. 4 Average crystallite size calculation acquired from Rietveld Refinement.	20
Table. 5 Specific capacity values for all symmetric supercapacitors at 200 mV/s	33
Table. 6 Specific capacity values for Bulk and Nano Symmetric Supercapacitors	34
Table. 7 Specific capacity, energy density, and power density values with respect to scan rates for asymmetrical supercapacitors that made with bulk and nano zinc oxides / AC.....	35
Table. 8 Specific capacity, energy density, and power density values with respect to scan rates for asymmetrical supercapacitor that made with ZN/TA & ZA/HBA.....	38

1. INTRODUCTION

In the realm of contemporary energy research, supercapacitors have emerged as a forefront technology, captivating researchers, and industries alike due to their unique set of advantages in the energy storage field. As the demand for sustainable and high-performance energy storage solutions intensifies, supercapacitors have gathered attention for their ability to bridge the gap between conventional batteries and capacitors. Their key attributes, such as rapid charge and discharge capabilities, extended cycle life, and high-power density, position them as promising candidates for addressing the limitations of traditional energy storage devices. [1]. Furthermore, it is imperative to underscore the profound influence of nanotechnology on the landscape of supercapacitor applications, emerging as the most captivating technological frontier of the twenty-first century [1]. Within this paradigm, metal oxides play a pivotal role in augmenting the specific capacity and specific energy attributes of electrodes. Simultaneously, carbon nanostructures play a strategic role in optimizing not only the high specific power but also ensuring a prolonged cycling life for these supercapacitors [1]. This symbiotic relationship between nanotechnology and supercapacitor design signifies a paradigm shift, presenting unprecedented opportunities for advancing energy storage capabilities. An effective technique to improve electrochemical performance is through the hybridization of carbon materials with different metal oxides, such as NiO, FeO_x and ZnO [2-4]. In this domain, ZnO nanoparticles find frequent application owing to their remarkable characteristics, encompassing anti-corrosive properties, superior heat resistance, elevated thermal and chemical stability, commendable oxidation resistance, ultraviolet shielding capabilities, a high refractive index, cost-effectiveness, substantial theoretical energy density, and heightened conductivity [5]. It has strong transmittance on the 0.4–2 (scale) optical wavelength range, a low optical pumping threshold value, and radiation resistance [6, 7]. ZnO has been used in optoelectronics with its extraordinarily broad bandgap (3.37 eV) and substantial exciton binding energy (60 meV) at ambient temperature [8]. The possession of a wide band gap offers numerous advantages, including high breakdown voltages, the ability to sustain substantial electric fields, reduced electronic noise, and the capability to handle elevated temperatures and power levels.

ZnO, typically displaying n-type characteristics, proves to be not only cost-effective but also biocompatible and ecologically safe, rendering it highly promising as a material for supercapacitor electrodes. Compared to many other transition metal oxides, including CoO (715 mAh g⁻¹), NiO (718 mAh g⁻¹), and CuO (674 mAh g⁻¹), ZnO has a greater theoretical capacity (978 mAh g⁻¹). Additionally, ZnO proves to be an excellent candidate for solid-state white illumination, given its high emission efficiency [9] and large band gap, necessitating ultraviolet light (387 nm) for activation [10]. In practical applications, the hydrophilic and photocatalytic characteristics of ZnO typically manifest concurrently, potentially leading to a combined hydrophilic self-cleaning or photocatalytic effect [11]. Moreover, ZnO finds diverse applications in areas such as photo printing, protective coatings, solar cells, blue laser diodes, supercapacitors, conductive thin-film LCDs, and electrophotography [12].

The performance of metal oxide in energy storage applications is greatly impacted by factors such as particle size, porosity, and electrical structure [13]. ZnO offers numerous advantages such as high surface area, chemical and photochemical stability, uniform pore size, shape selectivity, and diverse surface chemistry. The presence of a large surface area in ZnO enhances its surface activity, leading to improved performance in energy storage applications. [14]. The amount of porosity is directly affected by the production technique. The synthesis of ZnO nanomaterials can be achieved through various methods, each offering unique advantages and control over the morphology and size of the nanomaterials. Chemical vapor deposition (CVD) is a commonly used method for synthesizing ZnO nanomaterials, allowing precise control over the growth conditions and resulting in high-quality nanomaterials. The sol-gel method is another popular technique that offers simplicity and versatility in synthesizing ZnO nanomaterials with desired properties. Hydrothermal synthesis, which involves the reaction of precursors in a high-pressure aqueous solution, is also widely employed for the synthesis of ZnO nanomaterials. In comparison to the other methods described, the sol-gel process is the most widely used. The sol-gel process, which is the production method in this thesis, involves the hydrolysis and condensation of precursor molecules, typically metal alkoxides, in a solution to form a gel.

The gel is then subjected to a drying process, followed by calcination to obtain the desired ZnO nanomaterials. The sol-gel method allows for the manipulation of various parameters to tailor the morphology, size, and crystallinity of the resulting nanomaterials. Parameters such as precursor concentration, solvent composition, and pH can be adjusted to achieve the desired characteristics. This flexibility makes sol-gel synthesis an attractive choice for researchers and engineers. One of the key advantages of sol-gel synthesis is the ability to achieve low processing temperatures. This is particularly beneficial for materials that are sensitive to high temperatures. Additionally, the sol-gel method offers high purity in the synthesized materials, as impurities can be effectively removed during the gel formation and drying stages. Furthermore, sol-gel synthesis enables the incorporation of dopants into the ZnO nanomaterials. Dopants can modify the electrical, optical, and catalytic properties of the materials, expanding their potential applications. Moreover, the surface of the nanomaterials can be functionalized to enhance specific properties or enable compatibility with other materials or devices [15]. ZnO was chosen as the ideal material for supercapacitor electrodes due to its desirable characteristics. These include high conductivity, a large surface area, low density, significant porosity with the appropriate pore size, and a high capacitance-to-cost ratio.

Notably, ZnO has excellent chemical stability, and low cost. However, the practical application of ZnO in supercapacitors is often limited by its low electronic conductivity and poor cycling stability [48]. To overcome these limitations, complex ZnO materials often synthesized using solvent agents have been explored. The following is a detailed, sequential explanation of why this particular strategy is employed. First of all, the use of solvent agents enhances conductivity and electrochemical performance by facilitating the creation of complex ZnO structures like nanoparticles, nanorods, nanosheets, or nanostructured arrays. This increased complexity amplifies the surface area and porosity of the ZnO material, thereby improving its electrochemical performance.

This happens due to the provision of more active sites for charge storage, reduction in the ion diffusion path length, and an overall boost in conductivity. Secondly, the use of solvent agents to form complex ZnO structures contributes to improving the cycling stability of ZnO-based supercapacitors.

This is because the porous or nanostructured ZnO materials developed can withstand the strain brought about by repeated charge-discharge cycles, leading to enhanced cycling stability. Lastly, the versatility in material design is an added advantage of using solvent agents. This method allows for the precise adjustment of the size, shape, and morphology of ZnO structures. Consequently, it becomes possible to design materials with properties specifically tailored to meet the requirements of various applications [48]. To achieve these properties, the synthesis of ZnO particles involved the incorporation of tartaric acid, chitosan, ascorbic acid, and hydroxyl benzoic acid. The researchers specifically aimed to use cost-effective and environmentally friendly processes to ensure the commercial viability of the material [16].

Tartaric acid ($C_4H_6O_6$) was utilized in this work as the structure-directing agent to change the surface of ZnO particles because it is extremely water-soluble and can easily couple with Zn^{2+} ions [5,7,12]. By forming a complex with zinc ions, tartaric acid can help control the precipitation of ZnO, leading to smaller, more uniformly distributed particles. This can enhance the surface area and porosity of the resulting material, improving the charge storage capacity of the supercapacitor electrodes [37]. Chitosan (CS) is a natural polymer derived from chitin. It is often used as a stabilizing agent or template in the synthesis of metal oxide nanoparticles, including ZnO, due to its unique physical and chemical properties (e.g., cationic nature, biocompatibility, ability to form films). It has a high concentration of amino groups ($-NH_2$) as well as hydroxyl ($-OH$) groups that increase its capacity to interact with metal ions via ion exchange and electrostatic attraction [17]. The chitosan matrix can help control the size and distribution of the ZnO particles, leading to increased surface area which is beneficial for supercapacitor performance. Furthermore, chitosan can improve the mechanical stability of the electrode material [38]. Ascorbic acid ($C_6H_8O_6$) salt, also known as vitamin C, which is a plant-based reagent, was used as the corresponding redox molecules. Due to presence of the ascorbic acid, the metal ions could be maintained in the solution during the process [18, 19]. Ascorbic acid's redox reactions during the charging-discharge process can greatly improve the electrochemical performance of supercapacitors. Similar to the other reagents, ascorbic acid can also control particle size and distribution, leading to higher surface area and porosity, which are important factors for supercapacitor performance.

Furthermore, ascorbic acid is biocompatible and environmentally friendly, making it a preferred reagent for green synthesis [39]. 4-hydroxybenzoic acid ($C_7H_6O_3$) [HBA] is widely used in the synthesis of emulsifying agents, antioxidants, corrosion inhibitors, and food preservatives, as reducing and capping agents [20]. It can also help control the size and morphology of the particles, potentially leading to improved electrochemical performance. Additionally, the presence of hydroxybenzoic acid could enhance the stability of the ZnO, making it more suitable for long-term use in supercapacitors [40]. Due to the information given above, zinc sources of zinc acetate-dihydrate and zinc nitrate-tetrahydrate were utilized with tartaric acid, chitosan, ascorbic acid and hydroxybenzoic acid, in sol-gel production of particles to assess their effect on the crystal formation, therefore on the size and the morphology of synthesized ZnO. A thorough understanding of the structure and properties of ZnO at the nanoscale is crucial for optimizing its performance in these applications. To this end, various analytical methods such as X-ray Diffraction (XRD), Scanning Electron Microscopy (SEM), Raman Spectroscopy, Photoluminescent (PL) Spectroscopy, and Electron Paramagnetic Resonance (EPR) Spectroscopy have proven indispensable and were beneficial in this thesis study.

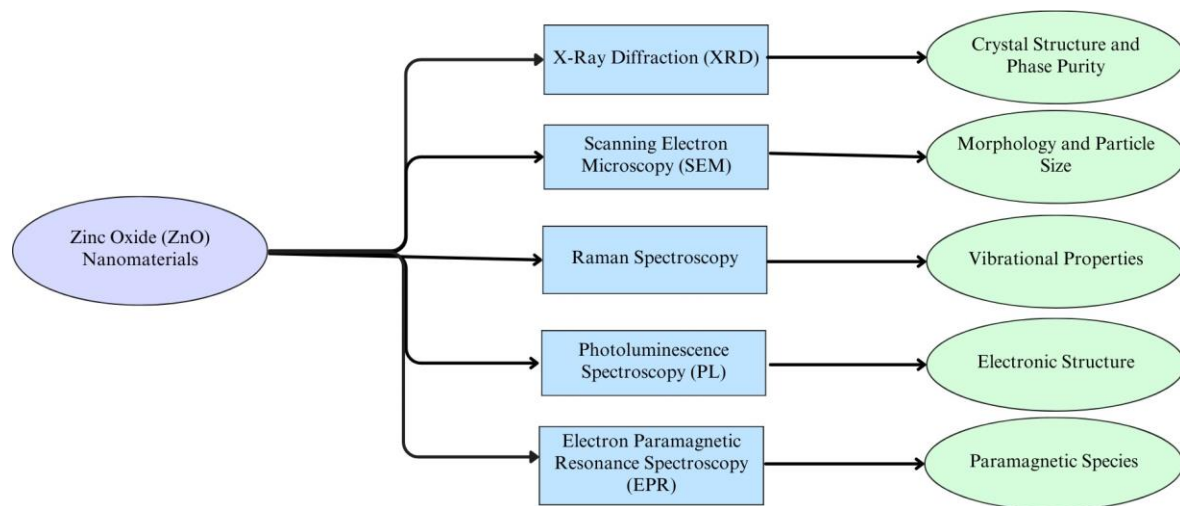


Fig. 1: Schematic diagram of analysis procedures of ZnO nanomaterials.

XRD provides information about the crystal structure and phase purity of ZnO nanomaterials, critical aspects when considering the electronic and optical properties of the material.

SEM, on the other hand, allows for the visualization of the morphology and particle size of the ZnO nanomaterials, key factors influencing surface area and, consequently, the material's reactivity and interaction with its environment [41,42]. Raman Spectroscopy provides insights into the vibrational properties of the ZnO nanomaterials, which can reveal defects and impurities that might impact the material's performance. PL Spectroscopy complements this by probing the electronic structure of the ZnO nanomaterials, providing information on energy band gaps and defects, essential for optoelectronic applications. Finally, EPR Spectroscopy allows for the detection of paramagnetic species, such as free radicals or defects, in the ZnO nanomaterials. These species could impact the electrical and optical properties of the material, affecting its suitability for various applications. Employing EPR is a powerful approach for examining the magnetic attributes of defect sites on a microscopic scale. The combination of EPR with optical spectroscopies offers a broader and more detailed insight into the overall structure of defects, particularly with respect to ZnO. Furthermore, when considering zinc oxide-based supercapacitors, these paramagnetic centers have a significant part to play. These centers are related to ionized Oxygen or Zinc vacancies manifesting within the ZnO crystal composition.

Their presence considerably sways the supercapacitor's performance by impacting its charge storage capability and electrical conductance. The repercussions of these paramagnetic centers are also elaborated in this thesis. The EPR method can efficiently explore and fine-tune these properties, thus enhancing the supercapacitor's performance. [43,44,45] In ZnO, there are four distinct types of point defects. Firstly, there can be a presence of missing zinc atoms, referred to as zinc vacancies. Secondly, zinc atoms may occupy positions where they are not supposed to be, known as zinc interstitials. The third possibility involves oxygen atoms being located in positions where they are not typically found, known as oxygen interstitials. Lastly, there can be a lack of oxygen atoms, known as oxygen vacancies. It is important to note that zinc interstitials are diamagnetic, meaning they do not respond to a magnetic field and cannot be detected using EPR. On the other hand, depending on their electron configuration, oxygen interstitials can exhibit paramagnetic properties and can be detected through EPR.

Oxygen vacancies, or missing oxygen atoms in ZnO, can exist in three different states. The first state is when an oxygen vacancy is empty, or it doesn't capture an electron. This results in a positive charge, and it doesn't exhibit a magnetic response, which is a state we call diamagnetic. The second state is when an oxygen vacancy captures one electron, which still results in a positive charge. However, due to the presence of an unpaired, or "free," electron, it exhibits magnetic properties and thus can be observed using EPR. The third state is when an oxygen vacancy traps two electrons. In this case, it can be diamagnetic, if the spins of both electrons balance each other. If the spins of both electrons do not balance each other it will be paramagnetic which again can be detected by EPR. There is a model called core-shell which needs to be explained within the concept of this thesis. This model essentially imagines ZnO nanoparticles as tiny spheres. Each sphere is made up of a core, which is covered by a layer that is called a shell, arranged in a hexagonal structure. This visualization is not just for the sake of imagination. It helps scientists understand how the size of these nanoparticles can affect their overall properties.

For example, by altering the thickness of the shell or the size of the core, we might see changes in the nanoparticles' reactivity, stability, or other physical and chemical properties [46,47]. Also, in a study, through the integration of data from EPR with PL impedance, and Raman spectroscopy analyses, it was detected that the defects within the core are primarily due to negatively charged vacancies of zinc atoms in the crystal lattice, and those on the shell are due to positively charged vacancies of oxygen atoms on the ZnO surface [51]. This also gives light to what was studied in this thesis. Similar outcomes were discussed in the scope of defect structures in ZnO materials. In essence, the combination of these analytical techniques allows for a comprehensive characterization of ZnO nanomaterials, enabling researchers to understand, and optimize these materials for specific applications, thus advancing the field of nanotechnology. Electrochemical measurements play a vital role in characterizing the performance and comprehending the behavior of supercapacitors made of ZnO. These measurements involve the use of a potentiostat and techniques like cyclic voltammetry (CV), electrochemical impedance spectroscopy (EIS), and galvanostatic cycling with potential limitation (GCPL). CV is a crucial technique that allows us to delve into the oxidizing and reducing behavior, as well as the capacitance of the ZnO electrodes.

It operates by gauging the current reaction in relation to the rate of change of the potential applied. This method provides pivotal data about the electrochemical interactions happening at the juncture of the electrode and electrolyte. This includes mechanisms of charge storage and the capacitive response. EIS is another important technique that gives insights into the impedance response of ZnO supercapacitors across a spectrum of frequencies. It offers valuable data, such as the resistance to charge transfer, the capacitance of the double layer, and the diffusion processes at the junction of the electrode and electrolyte. EIS is instrumental in deciphering the total electrochemical performance and can help highlight any potential constraints or degradation pathways. Lastly, GCPL is a method employed to assess the charge/discharge traits of ZnO supercapacitors. This technique furnishes information on specific capacitance, energy density, power density, and the stability of the cycling process. GCPL is beneficial in fine-tuning the composition of the electrode and electrolyte, the morphology of the electrode, and the mechanisms of charge storage.

This thesis embarks on a comprehensive study of the sol-gel production process of solvent agents, which will subsequently be incorporated into ZnO materials. The aim of this phase is to optimize the properties of the ZnO material, potentially improving its efficiency as an electrode in energy storage devices.

The main focus of this thesis can be summarized by following:

- The synthesis process of materials and conducting a series of rigorous characterization methods to study their structural, morphological, and compositional attributes.
 - XRD to investigate the crystalline structure
 - SEM to observe the morphology and surface characteristics
 - Raman Spectroscopy to understand the vibrational properties
 - PL to study the optical properties
 - EPR to analyze the paramagnetic defects of the materials
- These analyses will provide a comprehensive understanding of the material's properties following the incorporation of the solvent agents into the ZnO.

Upon successful characterization, the newly synthesized ZnO materials will be used as electrodes in symmetric supercapacitors. The performance of these supercapacitors will be evaluated through a series of electrochemical analyses, which will delve into their charge storage capacity and other crucial performance metrics. Subsequently, the two best-performing materials, determined by their electrochemical performance in the symmetric supercapacitors, will be selected for further experimentation. These materials will then be used as electrodes in asymmetric supercapacitors, a variant of supercapacitors that use two different materials for the two electrodes, potentially enhancing the device's overall performance.

Finally, a comparison of the electrochemical performance of the asymmetric supercapacitors will be conducted against supercapacitors using bulk and nano sized ZnO as electrodes. This comparison aims to evaluate the efficiency of the sol-gel process and the subsequent incorporation of solvent agents into the ZnO materials, thereby determining their suitability for use in advanced energy storage devices. This thesis is expected to provide valuable insights into the development and optimization of ZnO materials for energy storage applications, potentially paving the way for more efficient and sustainable energy storage solutions.

2. MATERIALS AND METHODS

2.1 Materials

Zinc Nitrate Tetrahydrate (Merck 108833 For Analysis Emsure, Zinc acetate dihydrate (Merck 108802 for analysis EMSURE, Tartaric Acid (Merck 100804 L (+)-For Analysis Emsure), Chitosan (448869 low molecular weight Emsure), 4-Hydroxybenzoic acid (ReagentPlus, $\geq 99\%$ Emsure), and Ascorbic acid (Merck 100468 L (+)-Ascorbic Acid for analysis EMSURE) were used from Sigma-Aldrich. Acetic acid is used as a solvent.

2.2 Synthesis of Nanoparticles with Sol-Gel Method

The process of fabricating powder specimens was executed through the sol-gel technique, employing a variety of initial materials. A comprehensive list of the compositions, outlining the combination of zinc precursors and additives that served as both reducing and capping agents for the synthesis of ZnO particles, is presented in Table 1. For the ZA/TA (Zinc Acetate-Tartaric Acid) sample, the procedure encompassed the dissolution of zinc acetate dihydrate in 100 ml of distilled water (DW) in a 250 ml beaker, followed by a gradual addition of tartaric acid. The resultant solution was continuously stirred using a magnetic stirrer for an hour until the temperature reached 90 °C. The mixture was then subjected to drying at 80 °C for a day and calcination in a muffle furnace at 500 °C for an hour. For the ZN/TA (Zinc Nitrate-Tartaric Acid) sample, the methodology mirrored that of the ZA/TA sample, except that the initial zinc source was zinc nitrate tetrahydrate. In the case of the ZA/Ch (Zinc Acetate-Chitosan) sample, both chitosan and zinc acetate dihydrate were individually added to 100 ml of DW and stirred magnetically.

Subsequently, 1 ml of acetic acid was gradually introduced into the mixture and stirred until uniformity was achieved. Lastly, the homogeneous solution was aliquoted into four 50 ml tubes and underwent two rounds of centrifugation at 4000 rpm for 10 min. to remove any precipitates. The powders obtained from the separation process were dried and calcined as previously described. In the case of the ZA/AA (Zinc Acetate-Ascorbic Acid) sample, separate solutions of ascorbic acid and zinc acetate dihydrate were prepared, and the ascorbic acid was gradually added drop by drop to the zinc acetate solution.

For the ZA/HBA (Zinc Acetate-Hydroxybenzoic Acid) sample, a solution of hydroxybenzoic acid was added dropwise to the zinc acetate solution, followed by drying and calcination. Afterward, the five different powder samples obtained were ground into a fine powder using an agate mortar and subjected to analysis. The experimental procedures can be found in Figure 2.

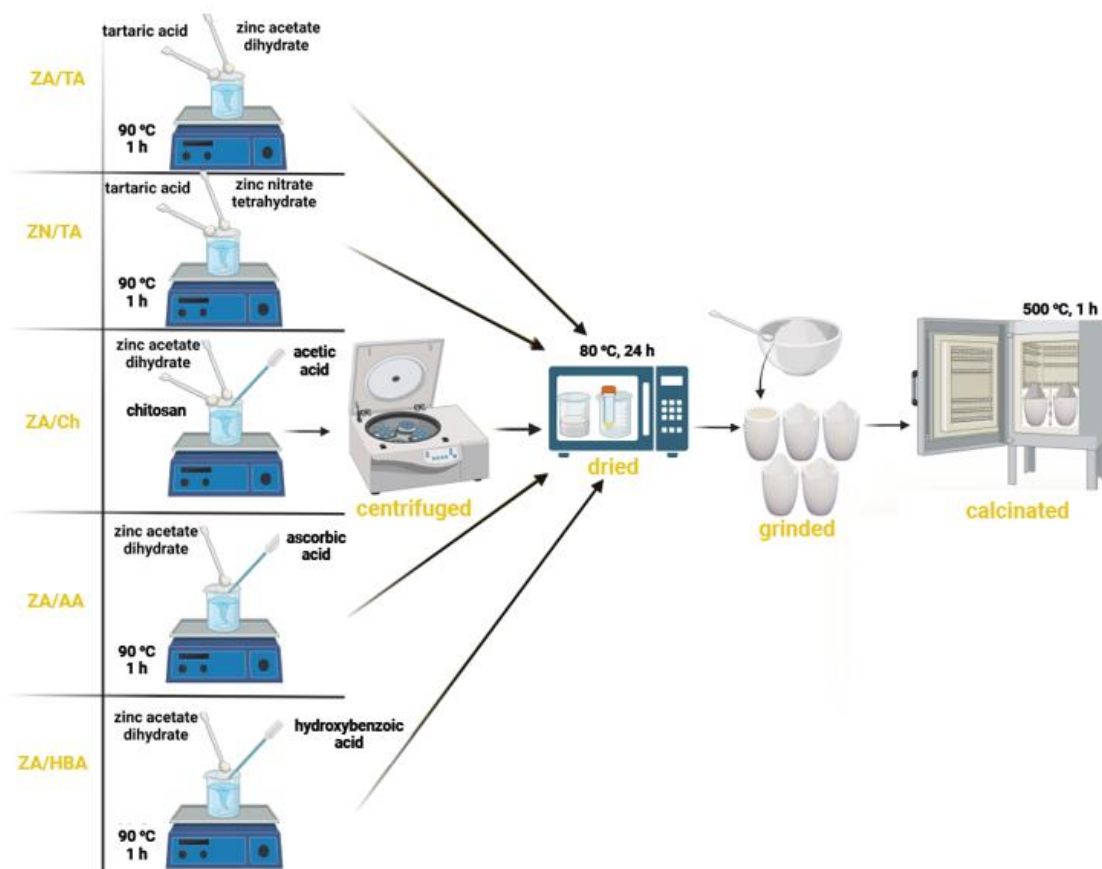


Fig. 2: Schematic diagram for experimental procedures of ZnO nanoparticles and drying, calcination temperatures- time values.

Table. 1 Powder samples, chemical compositions, starting materials, solvents, stirring, drying and calcination parameters used for the synthesis.

Exp.	Zinc Source	Reagents	Solvents	Stirring	Drying	Calcinating
ZA/TA	Zinc Acetate	Tartaric Acid	DW	90 °C, 1h	80 °C, 24 h	500 °C, 1 h
ZN/TA	Zinc Nitrate	Tartaric Acid	DW	90 °C, 1h	80 °C, 24 h	500 °C, 1 h
ZA/Ch	Zinc Acetate	Chitosan	DW + Acetic Acid	RT, centrifugal	80 °C, 24 h	500 °C, 1 h
ZA/AA	Zinc Acetate	Ascorbic Acid	DW	90 °C, 1h	80 °C, 24 h	500 °C, 1 h
ZA/HBA	Zinc Acetate	Hydroxy benzoic Acid	DW	90 °C, 1h	80 °C, 24 h	500 °C, 1 h

2.3 Production of Supercapacitors

To evaluate the electrochemical characteristics of the powder samples, a Potentiostat was employed to measure the properties. The Potentiostat is an instrument that regulates the voltage disparity between the two electrodes. In this particular case, the ZnO-based powders were utilized as both electrodes in the supercapacitor structure. Figure 3 displays the design of the supercapacitor, comprising two electrodes, a separator, and an electrolyte, which was employed in the project.

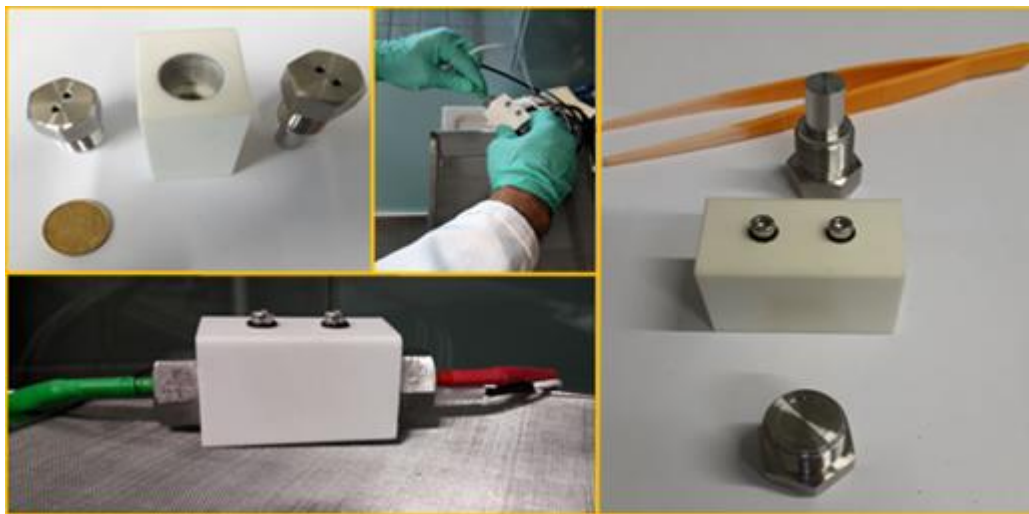


Fig. 3: Supercapacitor mounting device that was used in this thesis [49].

Throughout these experiments, a VMP 300 multi-potentiostat, a type of Biologic instrument, was put to use. The objective was to examine the electrochemical characteristics of the fabricated supercapacitors. Various testing methods were employed for this purpose, including EIS, CV, and GCPL experiments. These methods serve as tools to gauge the overall efficiency of the supercapacitors. Initially, the focus was on identifying the most efficient supercapacitor. To do this, symmetric supercapacitors were created, meaning both electrodes were made from the same samples. After comprehensive testing via EIS, CV, and GCPL two standout samples emerged, namely ZN/TA and ZA/HBA. These samples outperformed the rest in terms of electrochemical performance.

Subsequently, the high-performing ZN/TA and ZA/HBA samples were used to build new asymmetric supercapacitors, with active carbon serving as the other electrode. The choice of active carbon was not arbitrary. This material is widely used in supercapacitors because of its unique properties and advantages. Its large surface area and porous structure provide a broad area for electrolyte ions to engage, enhancing energy storage capabilities. As a result, supercapacitors exhibit higher capacitance values, meaning they can store and release energy more effectively. Active carbon is a favorite in the construction of supercapacitors due to its numerous benefits. Most notably, it has impressive electrical conductivity, which cuts down the internal resistance and boosts the rates at which charge is added or removed.

Furthermore, active carbon is chemically stable, meaning it can endure numerous cycles of charging and discharging without major wear and tear, leading to a longer lifespan. In this study, this material was put to use in a variety of tests. The setup for these tests was consistent across the board. It involved two electrodes separated by a glass fiber. A solution of 6 M potassium hydroxide (KOH) was used in conjunction with these components.

Table 2 below shows that all the initial symmetric supercapacitors - those with the same type of material on both electrodes - were set up with 3 mg of electrode material on each side, along with the 6 M KOH solution and a glass fiber separator. These supercapacitors were tested at a scan rate of 200mV/s, a measure of how quickly the voltage was changed during testing. Lastly, Table 2 also gives a glimpse of the various samples used in the creation of these symmetric supercapacitors.

Table. 2 Symmetric supercapacitor samples, mass of two electrodes. Also, electrolyte and separator names were given for the supercapacitor analysis of different ZnO nanoparticles.

	Electrode Materials	Mass of first electrode (mg)	Mass of second electrode (mg)	Electrolyte	Separator
Supercapacitor 1	ZA/TA	3	3	KOH (6M)	Glass Fiber
Supercapacitor 2	ZN/TA	3	3	KOH (6M)	Glass Fiber
Supercapacitor 3	ZA/Ch	3	3	KOH (6M)	Glass Fiber
Supercapacitor 4	ZA/AA	3	3	KOH (6M)	Glass Fiber
Supercapacitor 5	ZA/HBA	3	3	KOH (6M)	Glass Fiber

After analyzing the electrochemical data of all the symmetric supercapacitors, it was determined that the top performers were supercapacitors number 2 and 5, as indicated in Table 2. These two supercapacitors, which consisted of ZN/TA and ZA/HBA, were then used to create asymmetric supercapacitors. In this case, active carbon was applied to one electrode, and the electrode mass was set at 2mg each. The scan rate for the asymmetric supercapacitors was tested at 10 mV, 20 mV, 50 mV, 100 mV, and 200 mV for both samples.

2.4 Characterizations

2.4.1. X-ray Diffraction (XRD)

The synthesized ZnO nanoparticles were authenticated using the method of XRD, employing the Malvern PANalytical X-Pert PRO system specifically for this purpose. XRD patterns were captured with a diffractometer over an angle range from 20° to 80°, scanning at a rate of one degree per minute. The diffractometer made use of Cu K α 1 radiation, characterized by a wavelength (λ) of 1.54059 Å, and operated at a generator voltage and current of 60 kV. The Rietveld refinement method was conducted in this study for further examination. It is a method which is a powerful tool used in XRD studies for the quantitative analysis of crystalline materials. The Rietveld refinement method involves fitting a theoretical line profile, calculated based on a proposed crystal structure and other parameters, to the observed diffraction pattern. It considers various factors affecting the diffraction pattern. The method uses the least squares approach to minimize the difference between observed and calculated diffraction patterns [50].

2.4.2. Scanning Electron Microscopy (SEM)

SEM is a method used for detailed examination of microscopic regions and for understanding microstructural properties. The ZEISS Sigma 300 VP was utilized, operating at a working distance between 15–36 mm and an accelerating voltage ranging from 3-5 kV. The SEM images were visualized using ImageJ software. The SEM study included capturing images at both 5 and 1 μ m scales.

2.4.3. Raman Spectroscopy

Raman spectroscopy was utilized to investigate the lattice dynamics of ZnO nanostructures at a molecular level. The Renishaw Raman InVia System, along with a 532 nm green laser, was used to carry out the Raman spectroscopic studies. This sophisticated analytical approach facilitated an in-depth exploration of the molecular interactions within the ZnO nanostructures.

2.4.4. Photoluminescence Spectroscopy (PL)

PL spectroscopy was applied to all ZnO materials with the Edinburgh Instrument Spectrofluorometer FS5 to gain insights into their optical properties. The samples were exposed to 320 nm of excitation at room temperature with a slit distance for excitation and emission of 5 and 10 nm, respectively. PL spectroscopy can detect photoluminescent type defects, making it an analytical tool that provides vital information about the structural flaws in the materials.

2.4.5 Electron Paramagnetic Resonance Spectroscopy (EPR)

The EPR measurements were conducted using the Bruker EMX Nano, which features an integrated referencing system for the g-factor. The used microwave frequency was 9.63 GHz (X-band), and all measurements took place at room temperature. EPR spectroscopy stands as a highly effective instrument for recognizing paramagnetic flaw sites. These imperfections play a crucial role in enhancing the functionality of the electrode substance through elevation of its electrochemical actions [29].

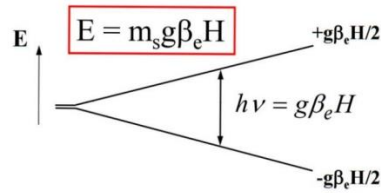


Fig. 4: Energy schema for Zeeman splitting [29].

By analyzing the g value in an EPR spectrum, researchers can unravel valuable information about the electronic structure, molecular surroundings, and even the type of paramagnetic species present. This insight enables a deeper understanding of the properties and behaviors of materials at the atomic and molecular level. Therefore, the g values for the nanoparticles that were produced were analyzed in the EPR spectrum with the Equation 1 given below.

When an external magnetic field is utilized to induce Zeeman splitting, it brings about the conditions required for resonance:

$$g_e = \frac{h \times \nu}{\beta_e \times H} \quad (1)$$

In the Equation 1 h represents Planck's constant, ν used to denote frequency of electromagnetic radiation, β_e stands for Bohr magneton, which is a physical constant and the natural unit for expressing the magnetic moment of an electron caused by either its orbital or spin angular momentum, and H is used to describe the magnetic field.

ZnO, like many materials, contains defects such as vacancies (missing atoms), interstitials (extra atoms), or substitutions (one type of atom replacing another). These defects can have unpaired electrons, making them detectable by EPR. By analyzing the EPR signals, one can identify the types of defects present in the material.

2.4.6 Electrochemistry

A Biologic VMP 300 multi-potentiostat was used to perform electrochemical measurements. To determine the electrochemical properties of the produced supercapacitors, various tests were conducted, including EIS, CV, GCPL experiments. These evaluation methods contribute significantly to the assessment of the supercapacitors' overall performance.

3. RESULTS AND DISCUSSION

3.1 X-ray Diffraction (XRD) Analysis

The produced ZnO nanoparticles' XRD patterns are displayed in Fig. 5 according to the JCDPS card no 36 1451. The hexagonal Wurtzite structure of the produced ZnO nanoparticles is confirmed by XRD [21].

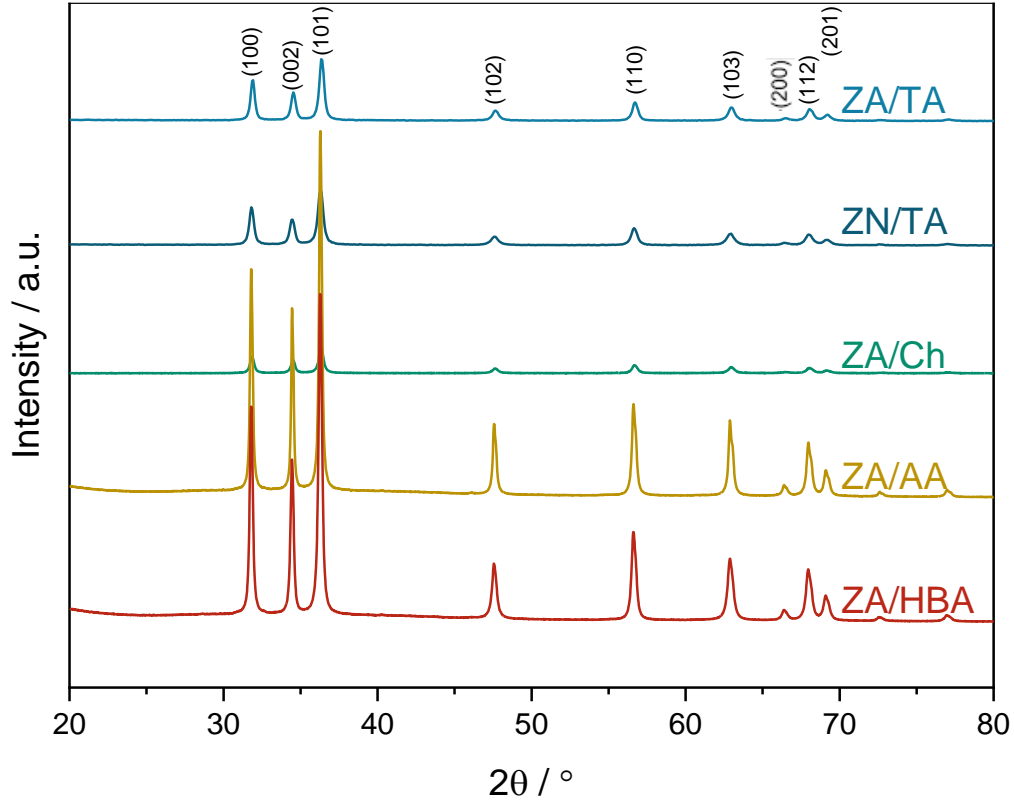


Fig. 5: XRD analysis of ZA/TA (a), ZN/TA (b), ZA/Ch (c), ZA/AA (d) and ZA/HBA (e) nanoparticles.

The presence of a hexagonal wurtzite structure indicated by the characteristic peaks related to (100), (002), (101), (102), (110), (103), (200), (112), (201) atomic planes has been confirmed. The degree of crystallization calculated within each sample is given in Table 4. The highest crystallinity is observed in the ZA/HBA sample which could be caused by the carbon elevation in the composition by use of HBA [21, 22]. The degree of crystallinity or amorphous percentage were calculated from the XRD patterns. After determining the crystalline peaks on the XRD graphs, degree of crystallinity is directly proportional to the total area under the crystalline peaks.

The degree of crystallinity can be calculated by dividing the area under the crystalline peaks by the total area under the XRD pattern, then multiplying by 100 to convert to percentage. The amorphous percentage can then be calculated by subtracting the degree of crystallinity from 100%.

Table. 3 Percentage of crystallinity and amorphous values of different ZnO nanoparticles.

Samples	Crystallinity Values (%)	Amorphous Values (%)
ZA/TA	83.6	16.4
ZN/TA	82.3	17.7
ZA/Ch	81.7	18.3
ZA/AA	83.7	16.3
ZA/HBA	84.2	15.8

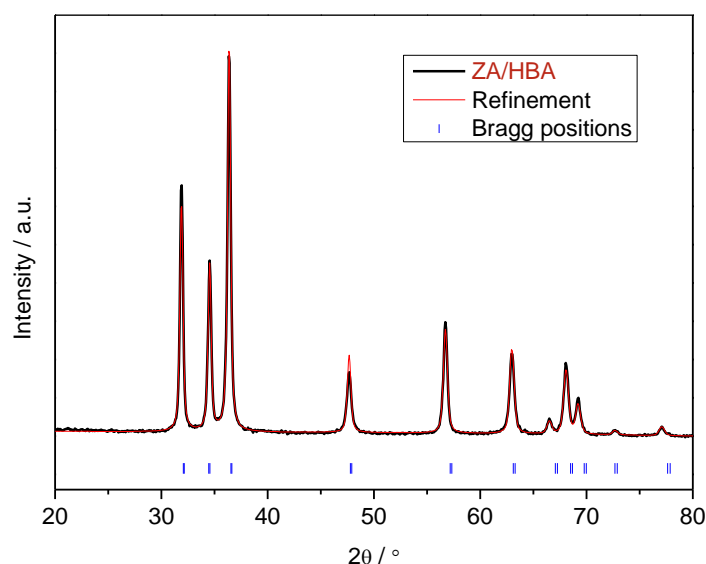


Fig. 5: Rietveld Refinement for sample ZA/HBA

Table. 4 Average crystallite size calculation acquired from Rietveld Refinement.

Sample No.	Symmetry	Lattice a (Å)	Lattice c (Å)	Cell Volume (nm ³)	Average Crystallite Size (nm)
ZA/TA	Hexagonal	3.25	5.21	55	48.1
ZN/TA	Hexagonal	3.25	5.21	55	41
ZA/Ch	Hexagonal	3.25	5.20	55	85
ZA/AA	Hexagonal	3.25	5.20	55	93
ZA/HBA	Hexagonal	3.25	5.21	55	71

Careful examination of the synthesized samples in relation to the calculated crystallinity ratios the distinct and intense peak at the Bragg positions in Table 4 provides further evidence that the ZA/HBA sample possesses the highest level of crystallinity compared to all the samples that were examined, as indicated by the XRD crystallinity results presented in Table 3. The exceptional structural stability and integrity of ZA/HBA ZnO nanoparticles are attributable to their well-ordered atomic arrangement within the crystal lattice, as evidenced by their high crystallinity. Furthermore, Rietveld Refining data revealed that ZA/AA possessed the highest average crystallite size. An increased dimension of the crystallites signifies a cohesive and all-encompassing crystal structure, which results in enhanced mechanical and electronic characteristics. In contrast to the ZA/AA sample, the decreased average crystallite size of the ZN/TA samples as determined by Rietveld Refinement data results in a less regular atomic structure and the potential for defects to manifest. The ZA/HBA sample, possessing the highest crystallinity according to the XRD results, exhibited the second-best specific capacitance, energy, and power density values. ZN/TA sample which has the least average crystallite size performed comparatively better electrochemically which confirms that less regular structure and a structure where defects can manifest is increasing electrochemical performance.

3.2 Scanning Electron Microscopy (SEM) Analysis

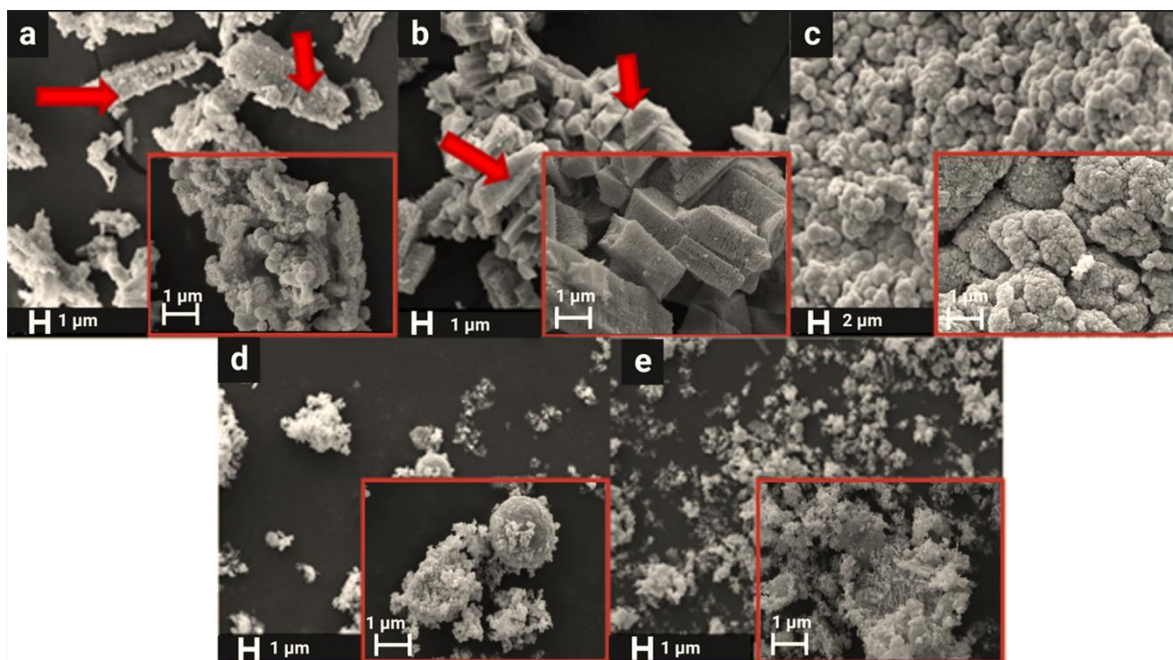


Fig. 6: SEM with 10.00 KX and 30.00 KX magnification of ZA/TA (a), ZN/TA (b), ZA/Ch (c), ZA/AA (d), ZA/HBA (e) nanoparticles.

The high-resolution SEM images taken at a magnification of 10,000 reveal that samples ZA/TA and ZN/TA display column-like structures with significant porosity between grains, as depicted in Fig. 6 (a) and (b).

Upon closer examination at 30,000 magnifications (outlined by the red rectangle), it is discernible that the ZA/TA sample comprises a combination of micron-sized spheres and extremely fine equiaxed nanostructures. The extent of the porous structures in the ZN/TA sample becomes evident at 30,000 magnifications, as shown in the inset of Fig. 6 (b). These porous structures could amplify electrochemical activity by offering a higher number of free surfaces. The SEM images indicate that introducing tartaric acid leads to the formation of column-like structures in Figs. 6(a) and (b), regardless of the zinc source. This might be due to the modification of the polar planes of the ZnO crystal when tartaric acid is added, which may trigger preferential growth [23]. According to existing research, tartaric acid behaves as a structure-directing agent. It has been documented those low concentrations of tartaric acid favor lateral growth, resulting in either hexagonal or spherical structures [23].

Contrastingly, high concentrations of tartaric acid promote directional growth, leading to the formation of smooth, one-dimensional structures [24, 25]. Fig. 6 (c) illustrates that combining zinc acetate with chitosan and acetic acid results in micron-sized globular structures in ZnO due to the presence of hydroxyl groups. At higher magnifications, nano-sized spherical crystals can be spotted on the surfaces of these globes. The use of ascorbic acid and hydroxybenzoic acid, on the other hand, encourages the development of feather-like fibrous structures, with the grown crystals being of nanometric scale, as displayed in Figs. 6 (d) and (e). As a consequence, both the starting materials and the additives alter the morphology, size, and crystallinity of the synthesized structures. These variations, in return, modify the corresponding surface areas and the porosity of the samples, which could be crucial in customizing the electrochemical properties of the electrodes. Electrochemical analysis and electron microscopy results demonstrated that the use of zinc nitrate as a zinc source generates greater porosity in the nanoparticle compared to zinc acetate, even though tartaric acid was used as the reagent at the same concentration, as illustrated in Fig. 6 (a) and Fig. 6 (b). The incorporation of chitosan in the ZA/Ch sample led to the formation of spherical structures, as shown in Fig .6 (c).

The SEM images of ZA/AA and ZA/HBA samples in Fig. 6 (d) and (e) also revealed that hydroxy benzoic acid resulted in the production of small nanoparticles, which in turn led to a better electrochemical response.

3.3 Raman Spectroscopy Analysis

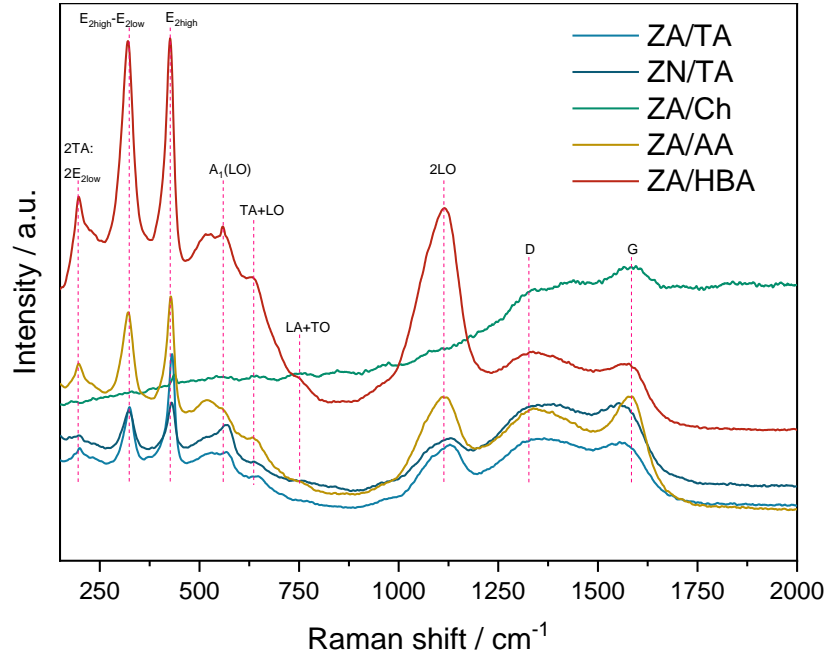


Fig. 7: First and second-order Raman spectrum of the synthesized particles ($\lambda = 532$ nm). The alterations in the vibration bands in the range of 125-2000 cm^{-1} are given.

Raman spectroscopy was employed to probe the lattice dynamics of ZnO nanostructures at the molecular level. Figure 7 highlights the Raman spectra, which confirms the successful synthesis of ZnO using various starting materials. In the hexagonal wurtzite (P63mc) ZnO structure, the count of phonons alters according to the number of atoms in the unit cell, culminating in a total of 12 phonons, three of which are acoustic [31].

A distinct peak around 430 cm^{-1} in Figure 7 is attributed to the $E_{2\text{high}}$ mode of ZnO, a characteristic Raman signature for wurtzite ZnO. While the $E_{2\text{low}}$ mode was not detected, the vibration at about 320 cm^{-1} is generally linked to a second-order Raman process, and it's ascribed to the $E_{2\text{high}}-E_{2\text{low}}$ difference mode [31,32].

In the Wurtzite structural arrangement, A1 and E1 phonon modes diverge, leading to the appearance of transverse optical (TO) and longitudinal optical (LO) phonons, a result of the structure's inherent polarity.

The activation of TO modes depends on the perpendicular alignment of incident and scattered light to the c-axis. Conversely, LO phonon modes become visible when incident and scattered light are parallel to the c-axis. Interestingly, a weak peak around 570 cm^{-1} is assigned to the A1(LO) mode. When the material's structure presents surface and/or aggregate defects, a second-order Raman process might occur, resulting in combination bands that represent the sum of frequencies derived from the optical branches. In this scenario, two-phonon difference modes are restricted to the frequency range of single-phonon branches. Conversely, frequencies exceeding approximately 600 cm^{-1} are governed by two-phonon sum modes and higher-order multi-phonon processes, as detailed in Figure 7 [33]. In addition to these spectral attributes, two unique characteristics were observed in the synthesized samples. These are the traces of carbon from the starting chemicals, believed to come from the sp^2 carbon domains, possibly indicating unbound carbon entities in the samples. The G-band's presence at 1590 cm^{-1} suggests C-C bond stretching, a distinctive feature of sp^2 carbon systems forming rings and chains. On the other hand, the appearance of the D-band around 1350 cm^{-1} depends on the presence of sp^2 carbons in disordered ring structures, and its emergence is affected by the composition and structure of these sp^2 carbon elements, as highlighted in previous studies [32,33].

3.4 Photoluminescent (PL) Spectroscopy Analysis

Figure 8 below presents the PL spectra for all five synthesized samples, with deconvolution performed to represent the peaks across different emission regions. All samples, as evident from the figure, exhibit defective structures due to their nanoscale size.

The first peak, noticeable in all the samples and located around 380 nm, corresponds to the bandgap energy of the samples. The subsequent broad peak is linked to the structural defects anticipated in ZnO samples.

The bandgap energy, which differs from one material to another, can be determined by using Equation 2, where E_g corresponds to the bandgap energy in eV, h denotes Planck's constant in eV.s, c represents the speed of light in m/s, and λ stands for wavelength in nanometers [26].

$$E_g = \frac{h \times c}{\lambda} = \frac{1240}{\lambda} \quad (2)$$

The standard bandgap energy for a ZnO sample ranges approximately from 3.1 eV to 3.4 eV. This large bandgap was observed in all five samples. With every sample displaying a peak around 380 nm, the bandgap energy was calculated using Equation 2, resulting in an energy of 3.2 eV. Deconvolution was also performed to identify the emission peaks in the visible range across all samples, yielding intriguing results as shown in between Figures 9-13. Visible emissions such as violet, blue, cyan, green, and yellow, typically observed in ZnO samples, are generally attributed to various intrinsic defects. These defects could include zinc interstitials (Zn_i) or vacancies (V_{Zn}), as well as oxygen interstitials (O_i) or vacancies (V_o). Green emission is reported to occur when the sample has oxygen vacancies as the dominant defect structure. Conversely, violet emission is documented when zinc interstitials are prevalent [34]. All of the samples exhibited clear violet emission, indicating the presence of zinc interstitials as a defect structure. However, samples ZN/TA and ZA/HBA, which demonstrated relatively superior electrochemical properties, exhibited lower emissions in the green wavelength zone which is visible in Figures 10 & 13.

The samples with fewer oxygen vacancies as one of the main defect structures showed better electrochemical properties. This suggests that the presence of oxygen vacancies as a defect structure might negatively impact the electrochemical properties.

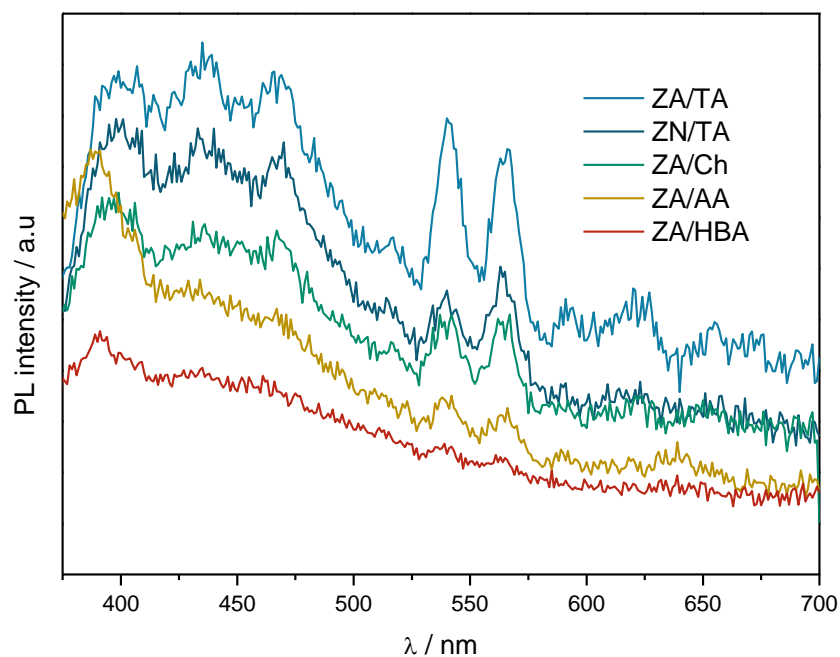


Fig. 8: PL spectra of ZnO samples ZA/TA, ZN/TA, ZA/Ch, ZA/AA, ZA/HBA

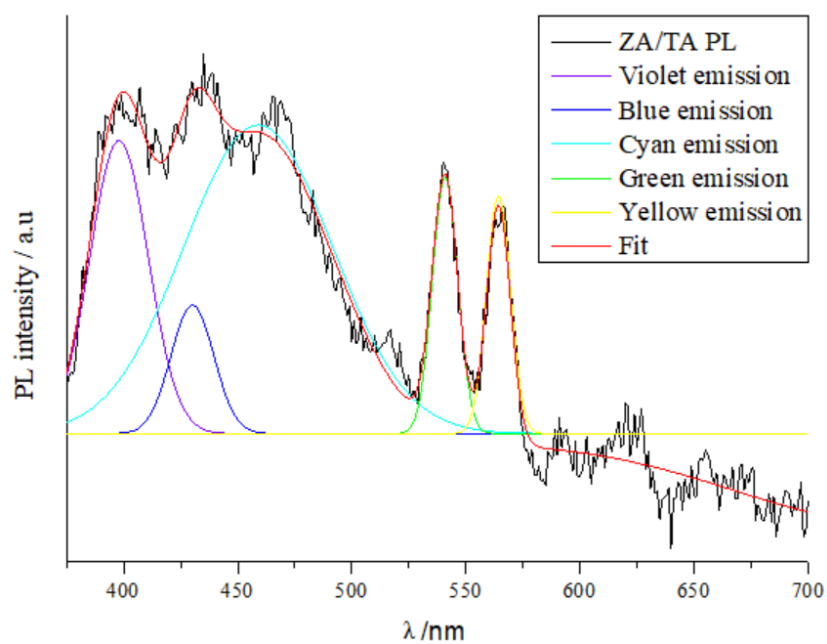


Fig. 9: PL spectra of ZA/TA with deconvolution

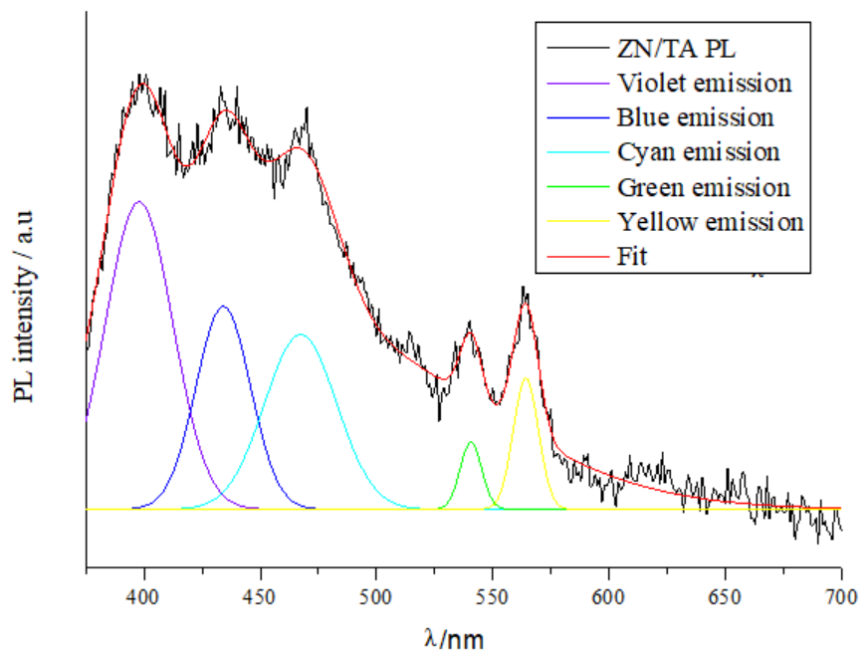


Fig. 10: PL spectra of ZN/TA with deconvolution

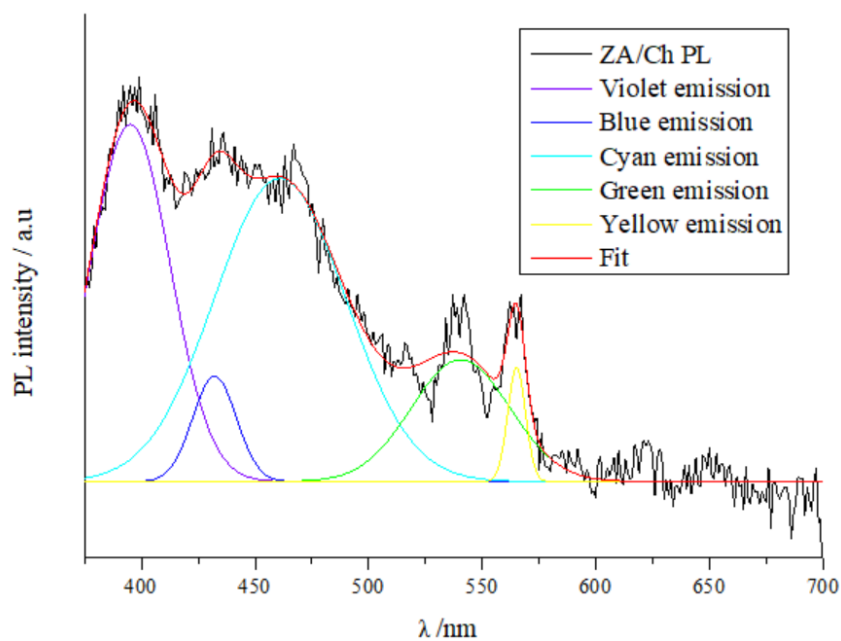


Fig. 11: PL spectra of ZN/Ch with deconvolution

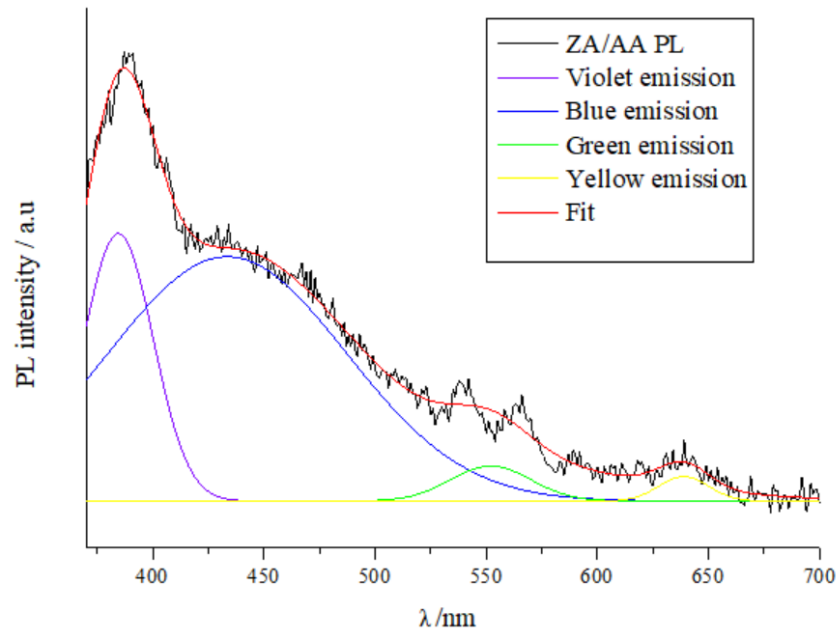


Fig. 12: PL spectra of ZN/AA with deconvolution

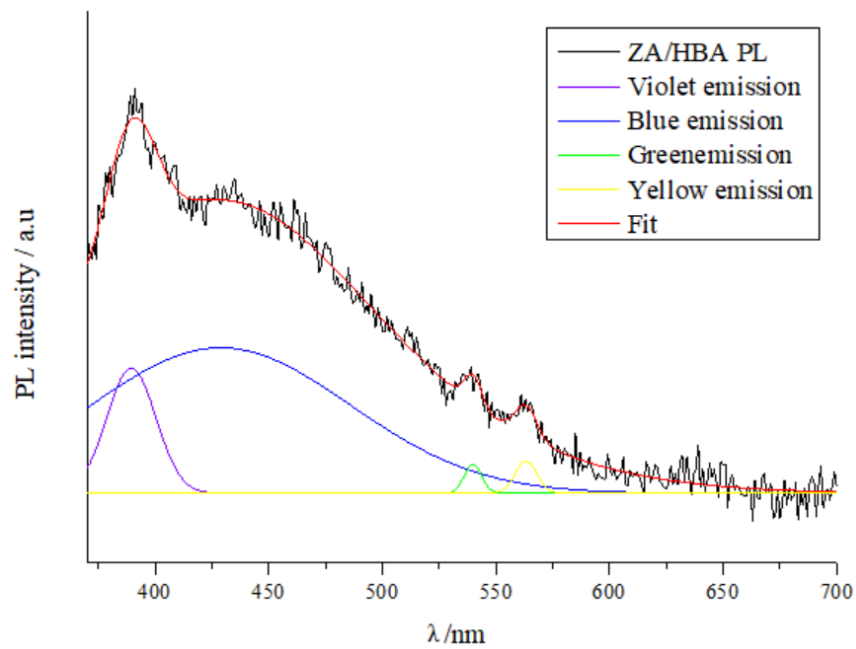


Fig. 13: PL spectra of ZN/HBA with deconvolution

3.5 Electron Paramagnetic Resonance (EPR) Spectroscopy Analysis

Figure 14 depicts the EPR spectrum of the nanoparticles, with the associated g values indicated. All of the materials exhibit both surface and core defects in the spectrum, except for material ZA/AA, which only displays surface defects in its EPR spectra. Based on various EPR studies, it has been established that two major types of intrinsic paramagnetic defects are applicable to ZnO structures. These resonate at $g \cong 1.96$ and $g \cong 2.003$, corresponding to core and surface defects, respectively [30]. Based on the described properties of ZnO, the emergence of these defects could be attributed to either the vacancy or the interstitial of oxygen or zinc atoms. The g value, as determined from the EPR spectra, provides information on the whereabouts of these imperfections within the material.

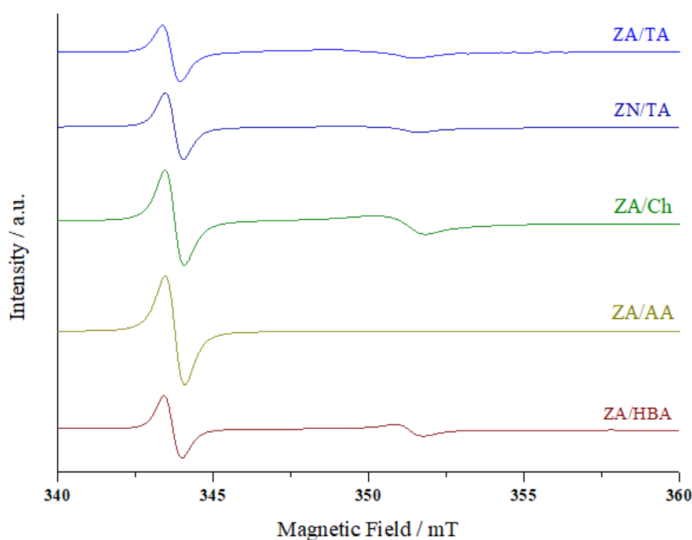


Fig. 14: EPR spectroscopy analysis of ZA/TA (a), ZN/TA (b), ZA/Ch (c), ZA/AA (d) and ZA/HBA (e).

The presence of a peak only at the surface g value in the EPR spectra of ZA/AA can be explained by the dominance of surface defects in this material, which obscures the spectra's representation of core defects. Although core defects are indeed present in the material, they are significantly overshadowed by surface defects.

In the research conducted by Erdem E. [51], the EPR analysis revealed distinct peaks at a g value of approximately 2.003, indicative of surface defects primarily due to oxygen vacancies. This finding strongly suggests that oxygen vacancies are a predominant defect structure within ZA/AA nanoparticles, more so than other types of defects. Subsequent electrochemical evaluations of these nanoparticles, details of which will be discussed in the following chapter, demonstrated that the ZA/AA nanoparticles exhibit mediocre performance. This outcome implies that the presence of oxygen vacancies is detrimental to the electrochemical efficacy of the nanoparticles. In light of these findings, it is proposed that future research should focus on optimizing the EPR spectrum to emphasize peaks associated with core defects. Such a shift could potentially improve the overall performance of the nanoparticles by mitigating the impact of surface defects and providing a clearer understanding of the role of core defects in electrochemical processes.

4. ELECTROCHEMICAL ANALYSIS

The electrochemical data for symmetric supercapacitors are categorized based on the types of nanoparticles used. Fig. 15 displays the CV curve for each sample, measured at a scan rate of 200 mV/s. All the CV designs exhibit a quasi-rectangular shape, demonstrating mirror symmetry that suggests ideal capacitor behavior. Additionally, this indicates that the charge storage mechanism in this system is due to a combination of Faradaic reactions and electric double-layer capacitance. After the CV graphs for the supercapacitors have been generated, the specific capacitance (C_p) must be calculated to compare the electrochemical performances. C_p can be determined using Equation 3 as shown below. For the symmetrical samples, both the mass of the electrodes and the scan rates were kept constant. Therefore, it can be inferred that a larger area on the CV curves will result in a higher specific capacitance for that particular sample.

$$C_p = \frac{Area}{2 \times m(g) \times Scan\ Rate\ (V) \times Potential\ window\ (V)} \left(\frac{F}{g} \right) \quad (3)$$

Specific capacitance values for symmetric samples were calculated and shown in Table 5. According to the C_p values, the best two samples were picked as Supercapacitor 2 (ZN/TA) and Supercapacitor 5 (ZN/HBA).

Table. 5 Specific capacity values for the produced ZnO symmetric supercapacitors at 200 mV/s

	C_p (F/g)	E (Wh/kg)	P (kW/kg)
Supercapacitor 1 (ZA/TA)	20.7	2,9	546,6
Supercapacitor 2 (ZN/TA)	59.9	8,3	963,1
Supercapacitor 3 (ZN/Ch)	25.0	3,4	483,5
Supercapacitor 4 (ZA/AA)	14.5	2	553,5
Supercapacitor 5 (ZA/HBA)	45.0	6,2	648,8

Fig. 15 illustrates that the current values for samples ZN/TA and ZA/HBA are superior compared to the others, which is also why these samples exhibit the best specific capacitance values in symmetrically prepared supercapacitors. Fig. 16 displays the Nyquist plots for all supercapacitors. The lowest impedance values are recorded for samples ZN/TA and ZA/HBA, indicating better electrochemical performance. Therefore, both the Nyquist plots and CV graphs agree that the symmetrical supercapacitors produced from ZN/TA and ZA/HBA individually demonstrate the best electrochemical performance.

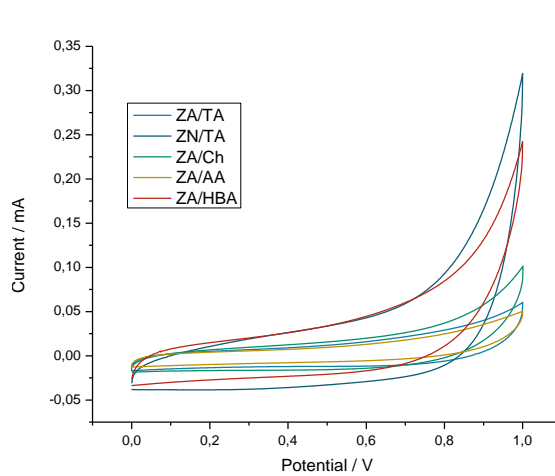


Fig. 15:CV Graph for symmetric supercapacitors at 200mV/s scan rate

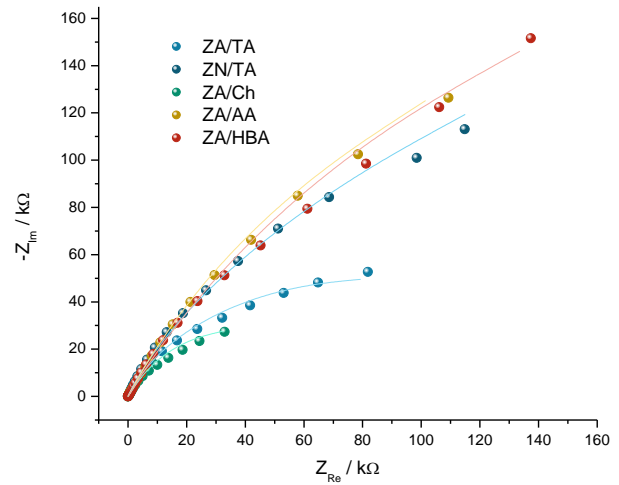


Fig. 16:Electrochemical impedance spectra (Nyquist plot) of supercapacitor designs.

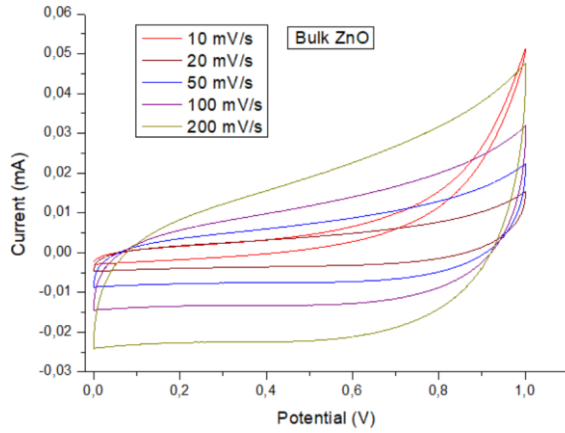


Fig. 17:CV Graph for symmetric bulk ZnO supercapacitors at various scan rates

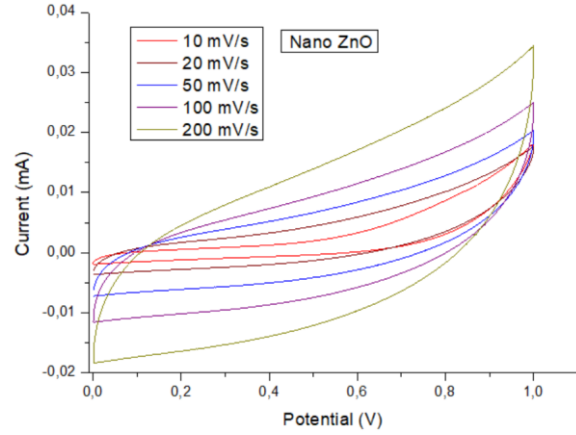


Fig. 18:CV Graph for symmetric nano sized ZnO supercapacitors at various scan rates

Table. 6 Specific capacity values for commercially used Bulk and Nano sized ZnO Symmetric Supercapacitors at 200 mV/s.

	Cp (F/g)	E (Wh/kg)	P(kW/kg)
Bulk ZnO (Symmetric)	30,5	4,2	837,1
Nano sized ZnO (Symmetric)	18,7	2,6	933,7

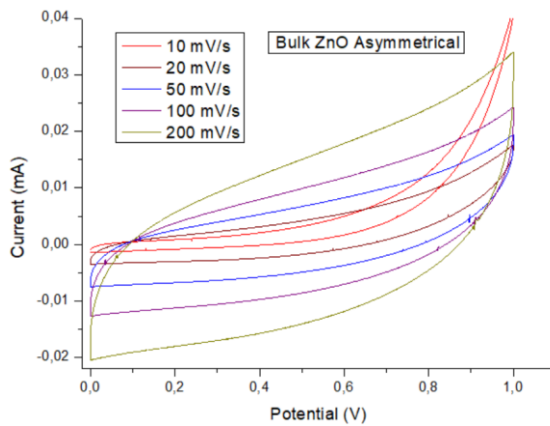


Fig. 19:CV Graph for asymmetric bulk ZnO supercapacitors at various scan rates

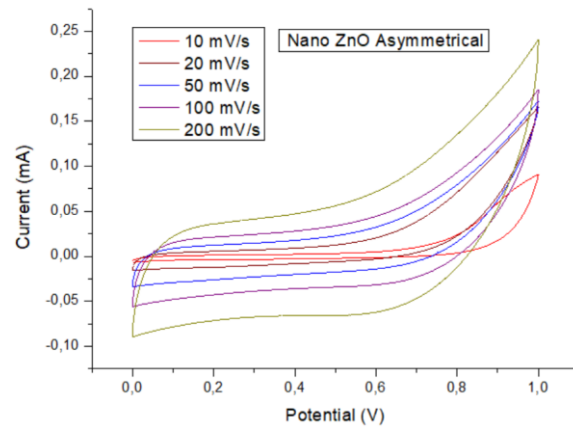


Fig. 20: CV Graph for asymmetric nano sized ZnO supercapacitors at various scan rates

Table. 7 Specific capacity, energy density, and power density values of asymmetrical supercapacitors. Supercap 1; Bulk ZnO/AC, Supercap 2; Nano ZnO/AC

	Scan Rate (mV/s)	Cp (F/g)	E (Wh/kg)	P (kW/kg)
Bulk ZnO/AC (Asymmetric)	10	70,5	9,8	798,2
Bulk ZnO/AC (Asymmetric)	20	64,9	9,0	735,1
Bulk ZnO/AC (Asymmetric)	50	50,6	7	572,3
Bulk ZnO/AC (Asymmetric)	100	40,2	5,6	454,9
Bulk ZnO/AC (Asymmetric)	200	31,7	4,4	359,4
Nano sized ZnO/AC (Asymmetric)	10	291,8	40,5	579
Nano sized ZnO/AC (Asymmetric)	20	324	45	642,9
Nano sized ZnO/AC (Asymmetric)	50	220,4	30,6	437,3
Nano sized ZnO/AC (Asymmetric)	100	175,2	24,3	347,6
Nano sized ZnO/AC (Asymmetric)	200	145,4	20,1	288,4

The raw materials for this experiment, namely the bulk and nano sized ZnO, were procured from a renowned supplier, Sigma Aldrich. These materials were then used to synthesize electrode materials, which were subsequently applied in the preparation of symmetric supercapacitors. To ensure a fair comparison, both categories of supercapacitors - one with bulk ZnO and the other with nano sized ZnO as electrodes - were crafted under identical conditions, keeping all other components of the supercapacitor constant.

For evaluating the electrochemical performance of these supercapacitors, CV graphs were plotted. Figure 17 represents the CV graph for the symmetric supercapacitor using bulk ZnO as the electrode. The calculated specific capacitance value was 30.47 F g^{-1} , measured at a scan rate of 200 mV/s. In a similar vein, the CV graph for the symmetric supercapacitor using nano sized ZnO as the electrode is represented in Figure 18. For this electrode configuration, the specific capacitance was found to be 18.67 F g^{-1} at the same scan rate of 200 mV/s. A comparative analysis with the data depicted in Table 6 (which represents the specific capacitance values for symmetric supercapacitors fabricated with different nanoparticles) reveals that the nano sized ZnO prepared in-house outperforms its bulk counterpart in terms of specific capacitance. Further, asymmetric supercapacitors were also fabricated, where bulk and nano sized ZnO's were used as the positive electrode (first electrode) and active carbon as the negative one (second electrode).

The CV graphs for these asymmetric supercapacitors were given in figures 19 and 20 for bulk and nano sized respectively. When the performance parameters were evaluated, the asymmetric supercapacitors with nano sized ZnO displayed superior qualities in terms of specific capacitance and energy density values. However, when these results were compared with the performance of asymmetric supercapacitors fabricated using sol-gel derived nanoparticles, they fell short. The specific data for these comparisons is presented in Table 8. Despite this, a significant inference drawn from the experimental data is the substantial improvement in power density values when using ZnO/reagent nanoparticles. The power density values obtained are at least five times higher than those obtained from commercially available zinc oxide-based supercapacitors, marking a crucial advancement in the pursuit of high-performance energy storage devices.

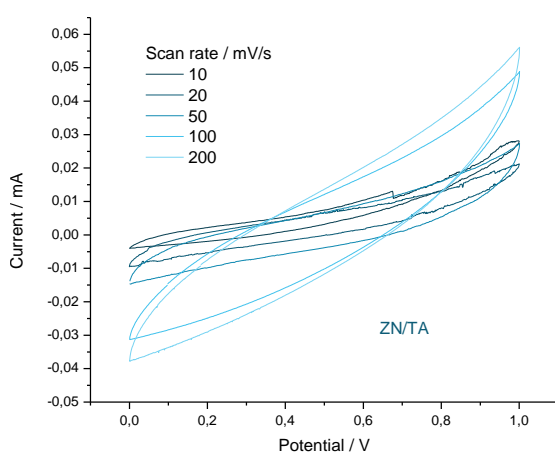


Fig. 21: CV graph for ZN/TA/AC asymmetric supercapacitor.

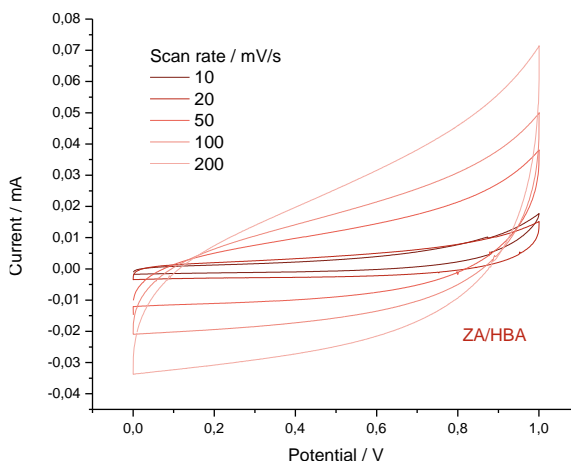


Fig. 22: CV graph for ZA/HBA/AC asymmetric supercapacitor.

From the two top-performing samples, asymmetric supercapacitors were produced using active carbon on one of the electrolytes. Fig. 21 presents the CV graphs for the asymmetric supercapacitor, which features ZN/TA on one electrode and active carbon on the other. Fig. 22 displays the CV graph for the asymmetric supercapacitor with ZA/HBA on one electrode and active carbon on the other. These CV graphs include results obtained from various scan rates, namely 10mV/s, 20mV/s, 50mV/s, 100 mV/s, and 200 mV/s.

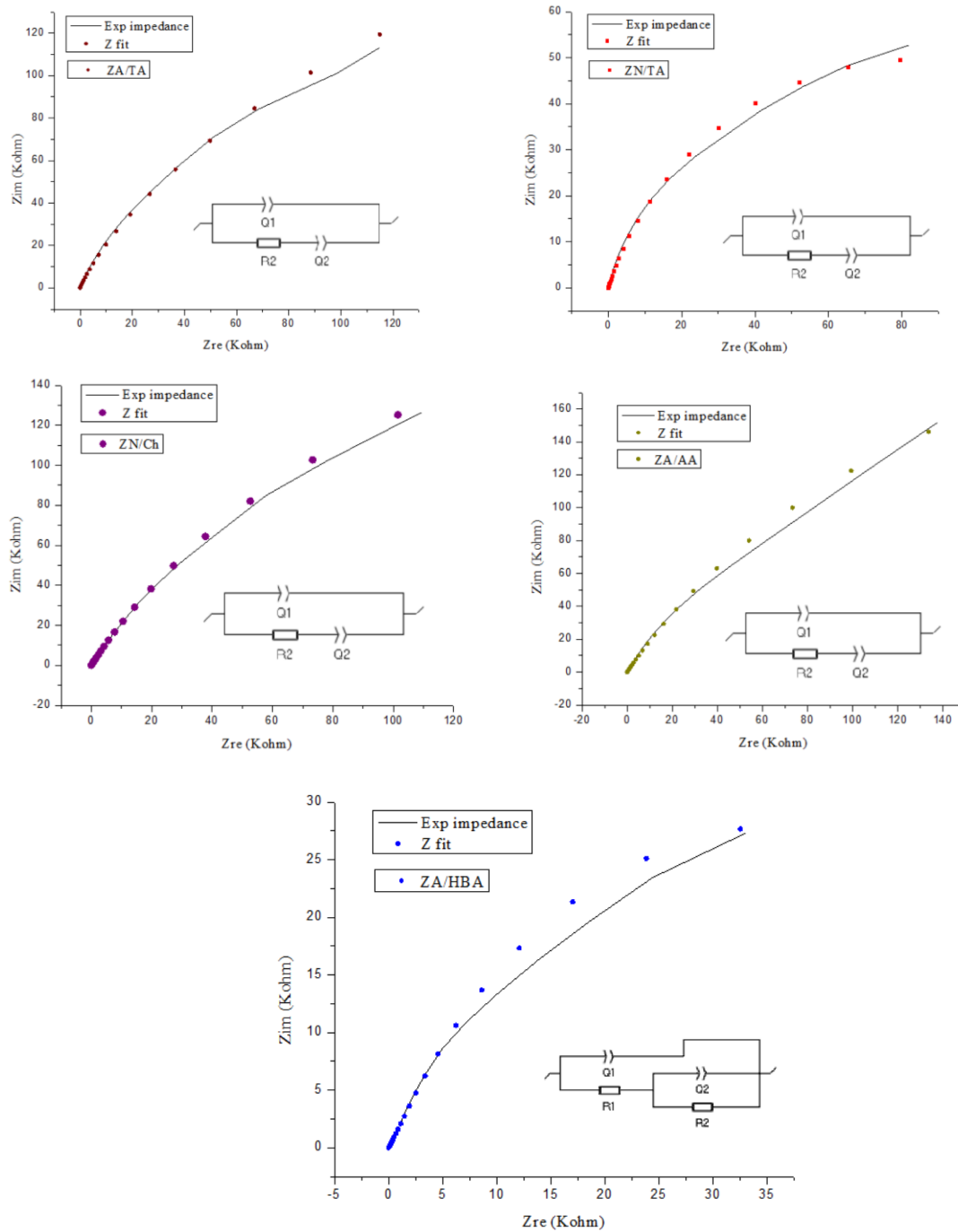


Fig. 23: Z-Fit graphs for samples ZA/TA, ZN/TA, ZA/Ch, ZA/AA, and ZA/HBA

Z fits were done in order to determine and draw the equivalent circuits for the symmetric supercapacitors which were prepared with samples ZA/TA, ZN/TA, ZA/Ch, ZA/AA, and ZA/HBA. The only different circuit found was the symmetric supercapacitor made with sample ZA/HBA as it is visible on figure 23 above.

Table. 8 Specific capacity, energy density, and power density values of asymmetrical supercapacitors. Supercap 1; Electrode 1: ZN/TA Electrode 2:AC, Supercap 2; Electrode 1:ZA/HBA Electrode 2:AC

	Scan Rate (mV/s)	Cp (F/g)	E (Wh/kg)	P (kW/kg)
ZN/TA/AC (Asymmetric)	10	88.0	12.2	4231.6
ZN/TA/AC (Asymmetric)	20	68.0	9.4	3269.4
ZN/TA/AC (Asymmetric)	50	46.9	6.5	2254.7
ZN/TA/AC (Asymmetric)	100	43.9	6.1	2112.0
ZN/TA/AC (Asymmetric)	200	26.2	3.6	1258.3
ZA/HBA/AC (Asymmetric)	10	89.7	12.5	698.6
ZA/HBA/AC (Asymmetric)	20	79.5	11.0	619.0
ZA/HBA/AC (Asymmetric)	50	92.8	12.9	723.1
ZA/HBA/AC (Asymmetric)	100	74.2	10.3	577.6
ZA/HBA/AC (Asymmetric)	200	56.2	7.8	437.5

Certain scan rates exhibit variations in specific capacitance values as they range from 10 to 200 mV/s. For instance, in ZA/HBA/AC, the peak Cp value is attained at a 50 mV/s scan rate. This can be attributed to the constructive interaction between the ZA/HBA and active carbon electrodes, suggesting that the asymmetric supercapacitor experiences more chemical reactions at a 50 mV/s scan rate compared to the others.

When the results in Table 8 are compared to the literature for ZnO supercapacitors [35,36,37], the self-assembled asymmetrical supercapacitors show a slightly higher specific capacity, a similar energy density, but notably larger power densities. All three aspects demonstrate impressive results for asymmetrical ZnO supercapacitors, with a maximum specific capacity of 88 F g⁻¹ for ZN/TA/AC and 92.8 F g⁻¹ for ZA/HBA/AC. Energy densities were calculated at a maximum of 12.2 Wh kg⁻¹ for ZN/TA/AC and 12.9 Wh kg⁻¹ for ZA/HBA/AC. Finally, power densities, which were the best aspect overall, were calculated at a maximum of 4231.6 kW kg⁻¹ for ZN/TA/AC and 723.1 Wh kg⁻¹ for ZA/HBA/AC.

Upon examining the electrochemical properties demonstrated in this study, it was observed that the sample labelled ZN/TA displayed the best capacitance, energy, and power density values. The elevated capacitance was presumed to be a result of the high porosity content and corresponding high surface area in this specific sample compared to the others. The electrochemical analysis concluded that zinc nitrate yielded better results than zinc acetate as a zinc starting material, and that tartaric acid outperformed the other reagents used in nanoparticle synthesis. The analysis suggested that hydroxy benzoic acid imparts superior electrochemical properties to the nanoparticle compared to ascorbic acid and chitosan, as it fostered the growth of nanofibers with a high degree of crystallinity.

5. CONCLUSIONS

To conclude, this thesis emphasizes the growing application of ZnO materials in supercapacitors. The focal point of the thesis is the creation, modification, and investigation of these materials, with a special emphasis on their flawed structure and electrochemical attributes. By highlighting the progress in the use of ZnO material, this study aids in the comprehension and advancement of more efficient and effective supercapacitors. The goal of the thesis was to contrast how crystallinity, porosity, and surface area alterations, based on the raw materials employed, translate into the energy storage potential of nanoparticles.

ZnO was chosen due to its superior electrode compatibility, cost-effectiveness, and easy production process. The reagents were selected for their plant-based, non-toxic, biocompatible, and thus environmentally friendly attributes.

Moreover, the utilization of the sol-gel method enabled the cost-effective, high-yield production of nanoparticles, which could be applied in supercapacitors. This thesis explored the optical attributes of ZnO materials using PL. By scrutinizing the light emissions, invaluable insights into the bandgap energies of these materials were acquired. This analysis has contributed to a deeper understanding of the electronic structure and behavior of ZnO. The prevalent defects within the materials were identified by analyzing them under the visible light emission range. The samples ZN/TA and ZA/HBA, which demonstrated superior electrochemical performance, showed no signs of oxygen vacancies as the dominant defects in their structure. This critical knowledge can guide the production of new ZnO materials with fewer oxygen vacancies as defects, which may be utilized as supercapacitor electrodes for improved electrochemical performance.

EPR analysis was conducted to comprehend the core-shell defect structure of ZnO materials. No significant differences that could explain the superior electrochemical performance were observed for samples ZN/TA and ZA/HBA. All of the samples exhibited core and shell defects, except ZA/AA which has only shown surface defect as a dominant defect in EPR. ZA/AA sample having shell defect as a dominant structure could be argued that it has oxygen vacancies as the dominant defect according to the literature [51].

As explained in PL results discussions, green emission corresponds to oxygen vacancies as defect structure in a material. Furthermore, the best electrochemically performing samples have shown fewer green emissions thus less oxygen vacancies. This also explains that ZA/AA will have worse electrochemical properties since the best performing samples have shown low signals of oxygen vacancies. In fact, it was found that among all samples ZA/AA had the worst electrochemical performance. In future studies, it could be argued that the EPR spectra that shows dominant surface g value peak hence oxygen vacancy dominance will result in poor electrochemical performance.

Lastly, electrochemical properties were inspected by preparing symmetrical and asymmetrical supercapacitors, with active carbon serving as the other electrode for the latter. The asymmetrical supercapacitors yielded remarkable results, especially in terms of power density values, when compared to the literature. As discussed, ZN/TA and ZA/HBA asymmetrical supercapacitors showed the best electrochemical performance among all the samples, which could be attributed to the absence of oxygen vacancies as a defect structure and the dominance of zinc interstitials.

According to the results, ZN/TA/AC supercapacitor and ZA/HBA/AC supercapacitor, which could be profitable and suitable candidates for commercial supercapacitors. They possess relatively high specific capacitance and large power density values. These are believed to be due to the high porous structure and rod-like shape of ZN/TA nanoparticles, and the very small nanostructure and high surface area of ZA/HBA nanoparticles. While tartaric acid renders the nanoparticle shape more porous and rod-like, hydroxybenzoic acid increases its surface area by minimizing its size to nano. Additionally, the sol-gel method utilized in this project represents a cost-effective production method, just like the raw materials used in supercapacitors. Moreover, the reagents in the materials, tartaric acid, and hydroxybenzoic acid, are non-toxic and biocompatible, which will be a critical consideration for humanity in the forthcoming years.

6. REFERENCES

- [1] Burcu Üstün, Hamide Aydın, Serkan Naci Koç, Ümran Kurtan, Amorphous ZnO@S-doped carbon composite nanofiber for use in asymmetric supercapacitors, *Diamond and Related Materials*, Volume 136, 2023, 110048, ISSN 0925-9635, <https://doi.org/10.1016/j.diamond.2023.110048>.
- [2] Z. Li, J. Bu, C. Zhang, L. Cheng, D. Pan, Z. Chen, M. Wu, Electrospun carbon nanofibers embedded with MOF-derived N-doped porous carbon and ZnO quantum dots for asymmetric flexible supercapacitors, *New J. Chem.* 45 (2021) 10672–10682, <https://doi.org/10.1039/d1nj01369f>.
- [3] W. Wang, S. Jiao, J. Cao, H.E. Naguib, Zinc oxide/carbon nanotube nanocomposite for high-performance flexible supercapacitor with sensing ability, *Electrochim. Acta* 350 (2020), 136353, <https://doi.org/10.1016/j.electacta.2020.136353>.
- [4] S. Shi, X. Zhuang, B. Cheng, X. Wang, Solution blowing of ZnO nanoflake-encapsulated carbon nanofibers as electrodes for supercapacitors, *J. Mater. Chem. A* 1 (2013) 13779–13788, <https://doi.org/10.1039/c3ta13247a>.
- [5] Muneer M. Ba-Abbad, Abdul Amir H. Kadhum, Abu Bakar Mohamad, Mohd S. Tariff, Kamaruzzaman Sopian. The effect of process parameters on the size of ZnO nanoparticles synthesized via the sol-gel technique, *Journal of Alloys and Compounds*, Volume 550, 2013, Pages 63-70, ISSN 0925-8388, <https://doi.org/10.1016/j.jallcom.2012.09.076>.
- [6] M. Bijl, M.I. Irfana, S. Sreejamol, P. Shajesh, S. Ananthakumar, R.V. Mangalaraja, S. Anas, Tartaric Acid Mediated Gelation Synthesis of Zinc Oxide Nanoparticles and their Photocatalytic Activity, *Materials Today: Proceedings*, Volume 9, Part 3, 2019, Pages 560-567, ISSN 2214-7853, <https://doi.org/10.1016/j.matpr.2018.10.376>.
- [7] Mohan Reddy Pallavolu, Jyothi Nallapureddy, Ramesh Reddy Vallapureddy, Goddamn Neelima, Anil Kumar Yendluri, Tapas K. Mandal, Babu Pejjai, Sang W. Joo, Self-assembled and highly faceted growth of Mo and V doped ZnO nanoflowers for high-performance supercapacitors, *Journal of Alloys and Compounds*, Volume 886, 2021, 161234, ISSN 0925-8388, <https://doi.org/10.1016/j.jallcom.2021.161234>.
- [8] Neha Gondal, Effect of high temperature annealing on structural and defect associated properties on ZnO nanoparticles, *Materials Today: Proceedings*, Volume 37, Part 2, 2021, Pages 3056-3057, ISSN 2214-7853, <https://doi.org/10.1016/j.matpr.2020.09.009>.
- [9] Chayma Abed, Monahan Ben Ali, Ahmad Abbas, Habib Elhouichet, Growth, structural and optical properties of ZnO-ZnMgO-MgO nanocomposites and their photocatalytic activity under sunlight irradiation, *Materials Research Bulletin*, Volume 110, 2019, Pages 230- 238, ISSN 0025-5408, <https://doi.org/10.1016/j.materresbull.2018.10.041>.

- [10] Asma Tabib, Wiem Bouslama, Brigitte Sieber, Ahmed Added, Habib Elhouichet, Mokhtar Férid, Rabah Boukherroub, Structural and optical properties of Na doped ZnO nanocrystals: Application to solar photocatalysis, *Applied Surface Science*, Volume 396, 2017, Pages 1528-1538, ISSN 0169-4332, <https://doi.org/10.1016/j.apsusc.2016.11.204>.
- [11] Shu Wang Guo, Liang Zhang, Ruifang Zhang, Zhao Liu, Ling Huang, Yongzhi Liu, Yuqi Zhang, Controllable tartaric acid modified ZnO crystals and their modification-determined optical, superhydrophilic/hydrophilic, and photocatalytic properties, *Journal of Alloys and Compounds*, Volume 768, 2018, Pages 214-229, ISSN 0925-8388, <https://doi.org/10.1016/j.jallcom.2018.07.195>.
- [12] Xu, S., Wang, Z.L. One-dimensional ZnO nanostructures: Solution growth and functional properties. *Nano Res.* 4, 1013–1098 (2011). <https://doi.org/10.1007/s12274-011-0160-7>
- [13] M. Siddique, N. Fayaz, and M. Saeed, “Synthesis, characterization, photocatalytic activity and gas sensing properties of zinc doped manganese oxide nanoparticles,” *Phys. B Condens. Matter*, p. 412504, Nov. 2020, doi: 10.1016/j.physb.2020.412504.
- [14] K. Sowri Babu, A. R. Reddy, C. Sujatha, K. V. Reddy, and A. N. Mallika, “Synthesis and optical characterization of porous ZnO,” *J. Adv. Ceram.*, vol. 2013, no. 3, pp. 260–265, doi: 10.1007/s40145-013-0069-6.
- [15] R. Mahdavi and S. S. Ashraf Talesh, “The effect of ultrasonic irradiation on the structure, morphology and photocatalytic performance of ZnO nanoparticles by sol-gel method,” *Ultrason. Sonochem.*, vol. 39, pp. 504–510, Nov. 2017, doi: 10.1016/j.ultsonch.2017.05.012.
- [16] K.R. Genwa, Anju Chouhan, Role of heterocyclic dye (Azur A) as a photosensitizer in photogalvanic cell for solar energy conversion and storage: NaLS–ascorbic acid system, *Solar Energy*, Volume 80, Issue 9, 2006, Pages 1213-1219, ISSN 0038-092X, <https://doi.org/10.1016/j.solener.2005.06.020>.
- [17] V. Vimala, L. Cindrella, Binder-free polymer material embedded in chitosan matrix for electrochemical energy storage devices, *Chemical Physics Letters*, Volume 809, 2022, 140172, ISSN 0009-2614, <https://doi.org/10.1016/j.cplett.2022.140172>.
- [18] Ragib Shakil, M. Nasiruzzaman Shaikh, Syed Shaheen Shah, Akter H. Reaz, Chanchal Kumar Roy, Al-Nakib Chowdhury, Md. Abdul Aziz, Development of a Novel Bio-based Redox Electrolyte using Pivalic Acid and Ascorbic Acid for the Activated Carbon-based Supercapacitor Fabrication, *Asian Journal of Organic Chemistry*, Volume 10, Issue 8, 2021, Pages 2220-2230, ISSN 2193-5807, <https://doi.org/10.1002/ajoc.202100314>.
- [19] A. Bronusiene, A. Popov, I. Barauskiene, I. Ancutiene, Effect of ascorbic acid on the properties of tin sulfide films for supercapacitor application, *Surfaces and Interfaces*, Volume 25, 2021, 101275, ISSN 2468-0230, <https://doi.org/10.1016/j.surfin.2021.101275>.
- [20] G. Bhanjana, G.R. Chaudhary, N. Dilbaghi, A. Kaushik, K.-H. Kim, S. Kumar, Probing of silver oxide nanoblades for 4-hydroxybenzoic acid quantification: a tool for food and water safety assessment, *Materials Today Chemistry*, Volume 26, 2022, 101142, ISSN 2468-5194, <https://doi.org/10.1016/j.mtchem.2022.101142>.

- [21] K. Pradeep Raj, K. Sadayandi, Effect of temperature on structural, optical and photoluminescence studies on ZnO nanoparticles synthesized by the standard co-precipitation method, *Physica B: Condensed Matter*, Volume 487, 2016, Pages 1-7, ISSN 0921-4526, <https://doi.org/10.1016/j.physb.2016.01.020>
- [22] [14] Xu, S., Wang, Z.L. One-dimensional ZnO nanostructures: Solution growth and functional properties. *Nano Res.* 4, 1013–1098 (2011). <https://doi.org/10.1007/s12274-011-0160-7>
- [23] Sumetha Suwanboon, Pongsaton Amornpitoksuk, Chamnan Random, Effect of tartaric acid as a structure-directing agent on different ZnO morphologies and their physical and photocatalytic properties, *Ceramics International*, Volume 45, Issue 2, Part A, 2019, Pages 2111-2116, ISSN 0272-8842, <https://doi.org/10.1016/j.ceramint.2018.10.116>.
- [24] M. Deeply, Ch. Srinivas, E. Ranjith Kumar, N. Krishna Mohan, C.L. Prajapat, T.V. Chandrasekhar Rao, Sher Singh Meena, Amit Kumar Verma, D.L. Sastry, XRD, EDX, FTIR and ESR spectroscopic studies of co-precipitated Mn–substituted Zn–ferrite nanoparticles, *Ceramics International*, Volume 45, Issue 6, 2019, Pages 8037-8044, ISSN 0272-8842, <https://doi.org/10.1016/j.ceramint.2019.01.029>.
- [25] J. Ungula, B.F. Dejene, Effect of solvent medium on the structural, morphological, and optical properties of ZnO nanoparticles synthesized by the sol–gel method, *Physica B: Condensed Matter*, Volume 480, 2016, Pages 26-30, ISSN 0921-4526, <https://doi.org/10.1016/j.physb.2015.10.007>.
- [26] Leighton, G. and Z. Huang, Accurate measurement of the piezoelectric coefficient of thin films by eliminating the substrate bending effect using spatial scanning laser vibrometry. *Smart Materials & Structures SMART MATER STRUCT*, 2010. 19. [27] Burke A. Ultracapacitors: why, how, and where is the technology. *Journal of Power Sources* . 2000;91:37–50.
- [28] Li Y Shang T Gao J Jin X Nitrogen-doped activated carbon/graphene composites as high-performance supercapacitor electrodes. *RSC Advances* . 2017;7:19098–19105.
- [29] Adrien Savoyant, M Rollo, M. Texier, R. Adam, S. Bernardini, et al.. Light-induced High-spin State in ZnO Nanoparticles. *Nanotechnology*, 2019, ff10.1088/1361-6528/ab57f1ff. fffhal-02321699f
- [30] Schumm M 2008. Ph.D. dissertation: ZnO-based semiconductors studied by Raman spectroscopy: semimagnetic alloying, doping, and nanostructures.
- [31] Toufani, M., Kasap, S., Tufani, A., Bakan, F., Weber, S., Erdem, E. (2020). Synergy of nano-ZnO and 3D-graphene foam electrodes for asymmetric supercapacitor devices. *Nanoscale*, 12(24), 12790-12800.
- [32] Ammar, A. U., Bakan-Misirlioglu, F., Aleinawi, M. H., Franzo, G., Condorelli, G. G., Yesilbag, F. N. T., Yesilbag, Y.O., Mirabella, S., Erdem, E. (2023). All-in-one supercapacitors with high performance enabled by Mn/Cu doped ZnO and MXene. *Materials Research Bulletin*, 165, 112334.
- [33] Ahn, C.H. et al. (2009) ‘A comparative analysis of deep level emission in ZnO layers deposited by various methods’, *Journal of Applied Physics*, 105(1). doi:10.1063/1.3054175.
- [34] Volkovich, Y.M. (2022) ‘Supercapacitors: Problems and prospects of development’, *Успехи химии*, 91(8). doi:10.1070/rcr5044.

- [35] Guo, G. et al. (2021) 'Preparation of lignin carbon/zinc oxide electrode material and its application in supercapacitors', *Molecules*, 26(12), p. 3554. doi:10.3390/molecules26123554.
- [36] POLAT, S. (2021) 'Production of znfe₂o₄ doped carbon cloth-based flexible composite electrodes for supercapacitors', *Türk Doğa ve Fen Dergisi*, 10(2), pp. 199–205. doi:10.46810/tdfd.953992.
- [37] Atar, N., et al. (2013). Synthesis of zinc oxide and its effect on the hydrogen evolution reaction of nickel in alkaline medium. *International Journal of Hydrogen Energy*, 38(34), 14396-14404).
- [38] Chen, X., et al. (2018). Chitosan-Based Polymer Matrixes for Fabrication of High-Performance Flexible All-Solid-State Supercapacitors. *ACS Applied Materials & Interfaces*, 10(50), 43457–43464.)
- [39] Ahmed, S., et al. (2016). Green synthesis of silver nanoparticles using *Azadirachta indica* aqueous leaf extract. *Journal of Radiation Research and Applied Sciences*, 9(1), 1-7).
- [40] Subramanian, B., et al. (2015). Green synthesis of zinc oxide nanoparticles using leaf extract of *Albizia lebbek* (L.) Benth. and their antifungal activity. *Asian Journal of Pharmaceutical and Clinical Research*, 8(1), 335-337).
- [41] S. K. Sharma, S. Dutta, and S. Sharma, "Structural, optical and morphological studies of ZnO nanoparticles," *Advanced Materials Letters*, vol. 3, no. 6, pp. 470–474, 2012.
- [42] D. Xiang, L. Han, R. Cai, X. Guo, and Z. Zhang, "Microwave-assisted synthesis of ZnO nanostructures and their photocatalytic properties," *Materials Letters*, vol. 65, no. 15–16, pp. 2439–2441, 2011.
- [43] N. Kumar, S. Sharma, R. K. Kotnala, and R. P. Tandon, "Raman spectroscopy and structural properties of nanocrystalline ZnO films," *Integrated Ferroelectrics*, vol. 138, no. 1, pp. 38–45, 2012.
- [44] A. Janotti, D. Segev, and C. G. Van de Walle, "Native point defects in ZnO," *Physical Review B*, vol. 76, no. 16, p. 165202, 2007.
- [45] "Defect-related properties of ZnO bulks, films, and nanostructures: A review," *Reports on Progress in Physics*, vol. 72, no. 11, p. 113501, 2009.
- [46] E. Erdem, K. Kiraz, M. Somer, and R.-A. Eichel, *J. Eur. Ceram.Soc.* 30, 289 (2010).
- [47] 2E. Erdem, H. C. Semmelhack, R. Bottcher, H. Rumpf, J. Banys, A. Matthes, H. J. Glasel, D. Hirsch, and E. Hartmann, *J. Phys.: Condens. Matter* 18, 3861 (2006)
- [48] Kumar, N. et al. (2022) 'Recent advanced supercapacitor: A review of storage mechanisms, electrode materials, modification, and Perspectives', *Nanomaterials*, 12(20), p. 3708. doi:10.3390/nano12203708.
- [49] Kasap, S. et al. (2019a) 'Superbat: Battery-like supercapacitor utilized by graphene foam and zinc oxide (zno) electrodes induced by structural defects', *Nanoscale Advances*, 1(7), pp. 2586–2597. doi:10.1039/c9na00199a.

[50] Paufler, P. (1995) 'R. A. Young (ed.). the Rietveld method. International Union of Crystallography. Oxford University Press 1993. 298 p. price £ 45.00. ISBN 0-19-855577-6', Crystal Research and Technology, 30(4), pp. 494-494. doi:10.1002/crat.2170300412.

[51] Erdem, E. 'Microwave power, temperature, atmospheric and light dependence of intrinsic defects in ZnO nanoparticles: A study of electron paramagnetic resonance (EPR) spectroscopy', Journal of Alloys and Compounds, Volume 605, 2014, Pages 34-44, ISSN 0925-8388, <https://doi.org/10.1016/j.jallcom.2014.03.157>.